Remote Sensing Applications: Society and Environment 39 (2025) 101623

Contents lists available at ScienceDirect

Remote Sensing Applications: Society and Environment

journal homepage: www.elsevier.com/locate/rsase

Massive increase of intertidal seagrass coverage in a large estuarine system revealed by four decades of Landsat imagery

Carlos A.S. Araújo [a,*], Simon Bélanger [a], Pascal Bernatchez [a], Mathieu Cusson [b]

[a] Département de biologie, chimie et géographie, Université du Québec à Rimouski, Rimouski, QC, G5L3A1, Canada
[b] Département des sciences fondamentales, Université du Québec à Chicoutimi, Chicoutimi, QC, G7H2B1, Canada

ARTICLE INFO

Keywords:
Eelgrass
Foundation species
Remote sensing
Subarctic
Nearshore environment
Google Earth Engine

ABSTRACT

The ecosystem services and functions of seagrass meadows are indisputable, and knowledge about their coverage is critical for coastal managers worldwide. In this study, the surface area coverage of the foundation species *Zostera marina* L. (eelgrass) was investigated in four contrasting subregions of the Estuary and Gulf of St. Lawrence (EGSL), eastern Canada. The meadows in all subregions mainly occupy intertidal zones. Our analysis covered broad spatial (meters to kilometers) and temporal (annual to decadal) scales and revealed unprecedented insights at a local and regional context. We processed surface reflectance products of the Landsat archive through the Google Earth Engine cloud computing platform. The processing scheme only considered emerged areas of intertidal zones from imagery acquired at the lowest tide levels because of inherent limitations imposed by water clarity and the poor radiometric quality for water applications of the early Landsat sensors. The polygons classified as eelgrass encompassed at least 25 % coverage of eelgrass for each patch, and the classification scheme showed a very good agreement with coastal ecosystem habitats maps generated by photointerpretation and field validation for the period between 2015 and 2019, with an overall accuracy of approximately 94 %. From the 40-year period analyzed (1984–2023), the meadows' surface area dramatically increased 10- (from approx. 0.3 to 2.5 km^2) to 21-fold (from approx. 0.8 to 16.7 km^2). The percentage of the intertidal area occupied by eelgrass meadows varied by subregion, ranging between 17 % and 82 %. In some subregions, meadows expanded landward. Some meadows experienced relatively short-term losses (interannual scale) in three subregions, although these losses differed in their timing. We propose several hypotheses involving hydrodynamic, sedimentological, drift ice and climatic processes that could explain long- and short-term variability of the meadow coverage. However, this complex relationship remains to be investigated. Overall, while showing suitable habitats for eelgrass colonization, this study also revealed the EGSL tidal flats as potentially important areas of biodiversity, carbon storage, and coastal protection against erosion.

1. Introduction

Seagrasses are recognized as foundation species, i.e., they modify their environments to create unique habitats, and constitute highly productive areas and biodiversity hotspots in coastal and nearshore environments globally (Duffy, 2006; Holmer, 2019). They

* Corresponding author.
E-mail addresses: sampca01@uqar.ca (C.A.S. Araújo), simon_belanger@uqar.ca (S. Bélanger), pascal_bernatchez@uqar.ca (P. Bernatchez), mathieu_cusson@uqac.ca (M. Cusson).

https://doi.org/10.1016/j.rsase.2025.101623
Received 23 October 2024; Received in revised form 14 May 2025; Accepted 8 June 2025
Available online 9 June 2025

provide valuable ecosystem services and functions (Henderson et al., 2019), such as offering habitat for various species including exploited ones (Beck et al., 2001; Whitfield, 2017; Unsworth et al., 2019b), protecting coastlines against erosion (Ondiviela et al., 2014), improving water quality (Moore, 2004), storing (blue) carbon (Duarte, 2017; Röhr et al., 2018). Seagrasses are significantly impacted by multiple stressors, including human activities (Hemminga and Duarte, 2000; Orth et al., 2006; Lotze et al., 2006) and climate change exacerbates these issues through rising sea temperatures and severe weather events (Duarte et al., 2018). Given these pressures, conservation and monitoring efforts targeting best management practices of seagrass meadows have been implemented worldwide (Grech et al., 2012; Unsworth et al., 2015, 2019a).

From a global perspective, seagrass meadows have declined in extent, although high variability in their distribution has been reported at regional and temporal scales (Waycott et al., 2009; Dunic et al., 2021). Gallagher et al. (2022) recently underscored the significant variability, with estimates of global seagrass coverage differing up to tenfold. This variability arises from the use of either a compiled and verified data set (McKenzie et al., 2020) or a predictive habitat model (Jayathilake and Costello, 2018), indicating a potential knowledge gap within the field. However, information about the distribution and extent of seagrass meadows is a minimum requirement for management practices, yet these baseline data are not publicly available in many coastal regions.

The heterogeneity of meadows at broad spatial scales, i.e., from meters to kilometers, is complexly related to ecological processes (seagrass landscapes; sensu Boström et al., 2006; Turner, 1989). At these spatial scales, yearly and decadal variations in the areal cover of seagrass meadows also have broad ecological relevance. In combination with fieldwork observations, space-borne Earth Observation Technologies (EOT) are the most reliable method for assessing information on seagrass at broad spatiotemporal scales (see reviews of Hossain and Hashim, 2019; Veettil et al., 2020).

Canada has the longest coastline in the world, and eelgrass (*Zostera marina* L.) meadows is a major habitat in 9 of its 12 bioregions (Murphy et al., 2021). In the Estuary and Gulf of St. Lawrence (EGSL), which connects the Great Lakes with the North Atlantic Ocean and encompasses one of the largest estuaries in the world (El-Sabh and Silverberg, 1990), eelgrass meadows were abundant. This littoral plant was harvested for commercialization (Michaud, 1985) before the "wasting disease", in the early twentieth century (see Den Hartog, 1987; Short et al., 1988). The disease is caused by a pathogen attributed to a marine slime mold-like protist, *Labyrinthula zosterae* Porter and Muehlstein (Muehlstein et al., 1991). This disease contributed to the near disappearance of most eelgrass meadows along the North Atlantic coast by the end of the 1920s. Punctual inventories and local knowledge have revealed the reappearance of eelgrass in nearshore waters of the EGSL at the end of the 20th century and relatively extensive meadows in recent years (e.g., Provencher and Deslandes, 2012; Jobin et al., 2021). Nonetheless, the distribution of eelgrass meadows in the EGSL at a broad spatiotemporal scale has not been reported.

We built a long-term data set of eelgrass distribution in four ecologically significant areas (subregions) of the EGSL to assess its spatial and areal changes over a 40-year time series. Our data set was built using the freely available Landsat imagery archive (Wulder et al., 2022) and a free cloud-computing platform (Google Earth Engine; Gorelick et al., 2017). Such a data set enables us to fulfill our main objective of describing the temporal trajectories of the eelgrass meadows of the EGSL by answering the following questions: What are the decadal trends in eelgrass cover in the EGSL? Are the trends similar across subregions? Do we observe linear trends, or is there significant interannual variability?

The four subregions selected within the EGSL were chosen based on their ecological importance, historical records of eelgrass presence, and availability of ancillary data, including field observations and regional studies. Although they are not spatially continuous, the selected areas span a gradient of environmental conditions, making them representative of the broader ecological heterogeneity found in the EGSL. This variability allows for comparative analysis of eelgrass dynamics under different local drivers. While our methodological approach leverages established remote sensing techniques, the main goal of this study is not methodological development, but rather the application of these tools to produce a robust, regionally contextualized assessment of long-term changes in eelgrass coverage. Our study thus serves as both a case application and a reference for future ecological monitoring in similar coastal environments.

2. Materials and methods

2.1. Study areas

The study sites (subregions; Fig. 1) are within temperate and subarctic zones, featuring a climate classified as cold, without a dry season, and with either warm or cold summers; however, these regions are experiencing a warming as per projections conditions (Köppen–Geiger classification; Beck et al., 2018a). These four subregions were chosen because eelgrass meadows are the dominant vegetated habitat present in relatively extensive tidal flats (Fig. 1B–E). Moreover, each subregion is subject to various environmental conditions, including the degree of wave exposure, circulation regimes, tidal ranges, and optical properties of water, and they are bordered by different types of coasts.

From downstream to upstream, or from northeast to southwest within the EGSL, the studied subregions are the Bay of Sept-Îles (BSI), the Manicouagan Peninsula (MAN), Rimouski Bay (RIB), and L'Isle-Verte Bay (IVE, which includes a National Wildlife Area of Canada). These subregions are characterized by large muddy to sandy tidal flats (Fig. 1), positioned in sheltered and fetch-limited locations unlike the central parts of the EGSL. The BSI eelgrass meadows are in a large and partially enclosed bay, whereas those of RIB and IVE are protected by an island. This sheltered coastal environment in these three subregions favors fine sedimentation and the development of salt marshes dominated by the smooth cordgrass (*Spartina alterniflora* Loisel), which often occupies the upper limit of the tidal flats. The MAN eelgrass meadows are much more directly exposed to waves and are bordered by sandy beaches and cliffs. Other depositional facies within the intertidal zones include deltas and tidal channels, which can also be colonized by eelgrass,

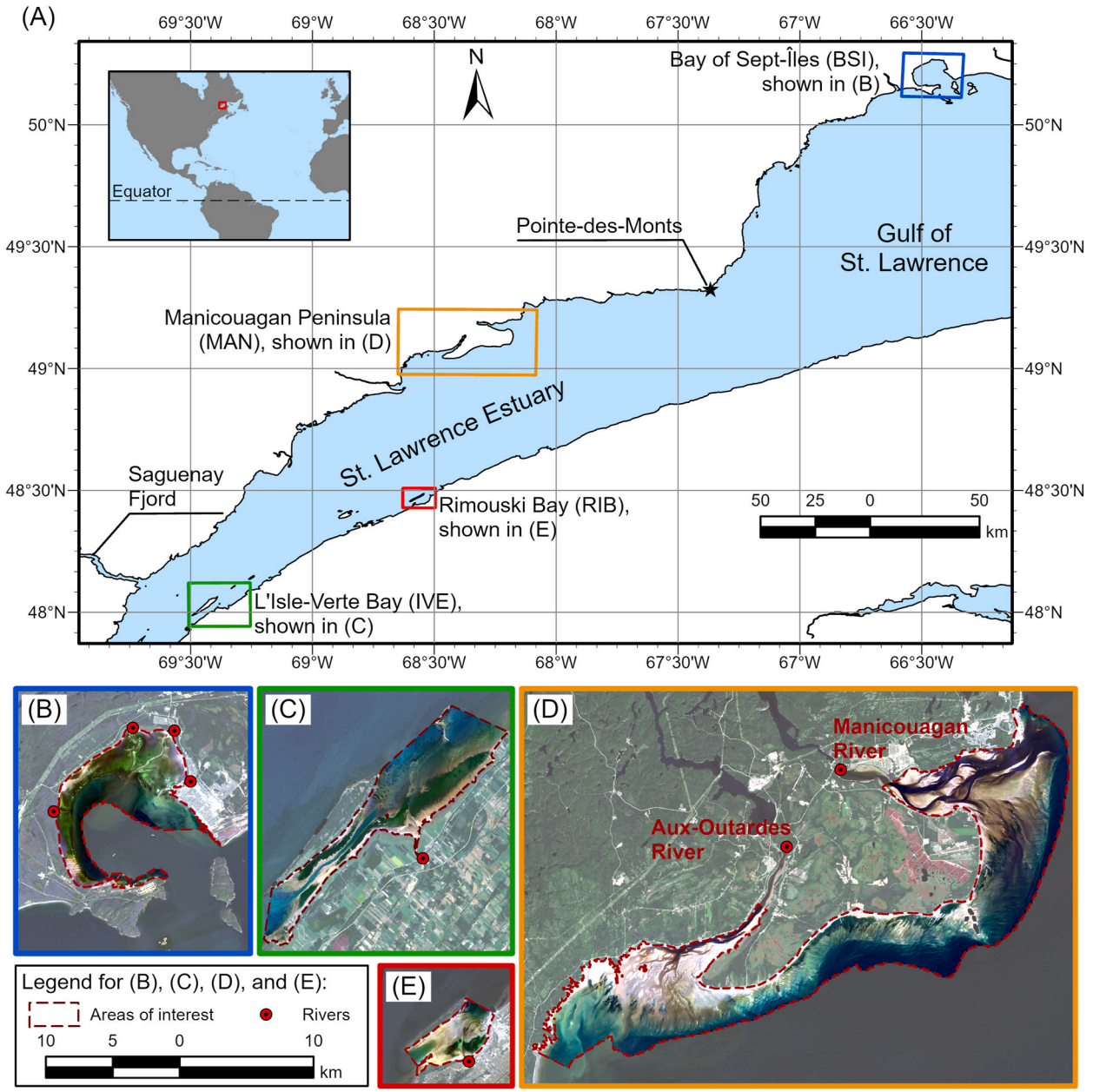

Fig. 1. (A) Study areas (subregions) in the Estuary and Gulf of St. Lawrence (EGSL). The inset shows the EGSL in North America context. Primary delimitation of areas of interest (red dashed lines) for the (B) Bay of Sept-Îles (BSI), (C) L'Isle-Verte Bay (IVE), (D) Manicouagan Peninsula (MAN), and Rimouski Bay (RIB). The main local riverine outlets are indicated for each subregion and the background images are a true-color composition of recent (2020s) Landsat 8 (or 9) OLI scenes (USGS L2SP).

especially in the MAN subregion. Scattered boulders and cobbles in BSI, RIB, and IVE, found in both intertidal and subtidal zones, support diverse and abundant macroalgal assemblages, and the heterogeneous seabed of the subtidal zones is more likely to be occupied by macroalgae than by other vegetated substrates (Quintin et al., 2006; Jobin et al., 2021; Ferrario et al., 2022; Légaré et al., 2022).

All four subregions are influenced by major and local riverine discharges. First, the waters in the nearshore zones of BSI are affected by four rivers that flow into the bay (Fig. 1B–Araújo and Bélanger, 2022; Shaw et al., 2022). Second, the area adjacent to the MAN is influenced by the plumes of the Aux-Outardes and Manicouagan rivers (Fig. 1D–Therriault et al., 1990). Finally, RIB and IVE, in addition to receiving waters from local riverine discharges, are also influenced by brackish waters that are flushed along the south shore, corresponding to the outflow of the Saguenay Fjord and the upper St. Lawrence Estuary (Fig. 1E and C; El-Sabh et al., 1982; Therriault et al., 1990). Therefore, different oceanographic conditions exist between the lower St. Lawrence Estuary, from

approximately the mouth of the Saguenay Fjord to Pointe-des-Monts, surrounding the MAN, RIB, and IVE, and the northern part of the Gulf of St. Lawrence, surrounding BSI (see Fig. 1A).

In the EGSL, the tides are predominantly semidiurnal, with daily inequalities, and fortnightly cycles with neap and spring tides being a marked feature (Fig. 2B). Neap and spring tide values for the BSI subregion typically range between 0.54 and 3.50 m, respectively (Shaw et al., 2022), but tidal amplitudes are higher upstream in the EGSL (see El-Sabh and Murty, 1990). Thus, in the MAN and RIB subregions the amplitudes will be higher than in the BSI subregion, and even higher in IVE, often reaching 5 m.

2.1.1. *Regional characteristics and rationale for image selection*

Knowledge of the variability of tides, water optical properties, and reflectance of nearshore vegetation is a primary requirement for mapping seagrass using optical approaches, including multispectral satellite imagery. In the EGSL, eelgrass meadows primarily occupy intertidal areas and, to a lesser extent, shallow subtidal zones (Jobin et al., 2021, Fig. 2A).

The optical properties of nearshore waters in the northern part of the EGSL are influenced by high concentrations of colored dissolved organic matter (CDOM) and moderate levels of suspended particulate matter (SPM), with an average of 10 mg L^{-1}) (Araújo and Bélanger, 2022). To illustrate the effects of optically significant constituents in the water of the EGSL, the spectral diffuse attenuation coefficient of downwelling irradiance ($K_d(\lambda)$) and the light penetration depth ($Z_{90}(\lambda)$; as defined by Gordon and McCluney, 1975) are shown in Fig. 2C (mean ± standard deviation). $K_d(\lambda)$ was calculated from 173 in situ profiles of the downwelling diffuse irradiance ($E_d(\lambda)$), using a Compact Optical Profiling System (C-OPS, Biospherical Instruments Inc., San Diego) collected during several

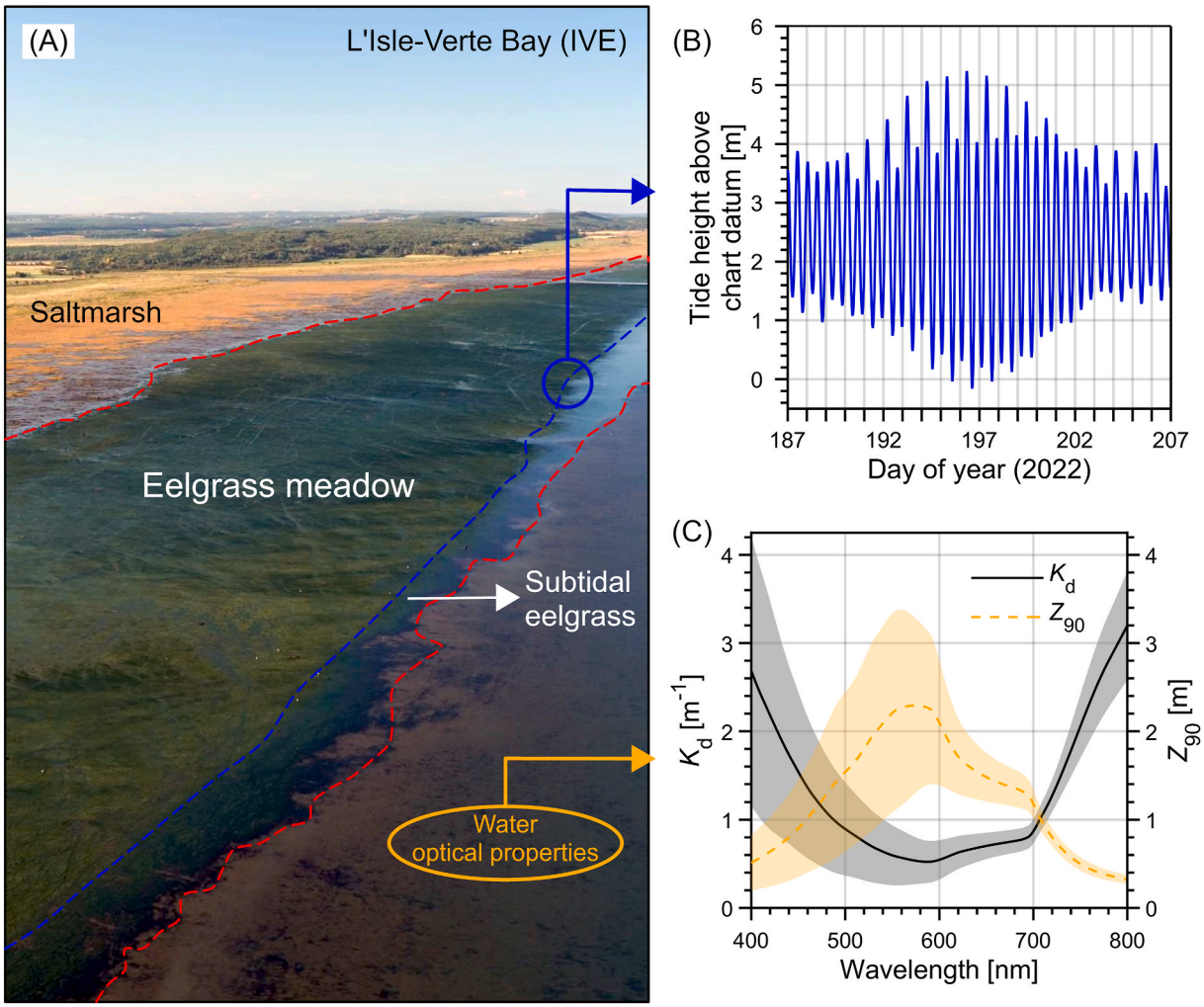

Fig. 2. General characteristics of eelgrass meadows in the Estuary and Gulf of St. Lawrence and the physical processes affecting their distribution. (A) Oblique aerial photograph taken in the L'Isle-Verte Bay subregion at low-tide conditions (image courtesy from the *Laboratoire de dynamique et de gestion intégrée des zones côtières, UQAR*). (B) Tidal variability for a 20-day period in 2022 (tidal gauge in Baie-Sainte-Catherine, at the mouth of the Saguenay Fjord—data available from the Canadian Hydrographic Service). (C) Some optical characteristics of the water column surrounding meadows: the spectral diffuse attenuation coefficient of downwelling irradiance ($K_d(\lambda)$) and the light penetration depth ($Z_{90}(\lambda)$). The solid and dashed lines indicate the mean values of K_d and Z_{90}, respectively, and the shaded areas indicate the (±) standard deviation.

field campaigns in the BSI and MAN subregions (for details, see Araújo et al., 2022; Araújo and Bélanger, 2022). The $K_d(\lambda)$ was then used to determine $Z_{90}(\lambda)$ as:

$$Z_{90}(\lambda) = \frac{1}{K_d(\lambda)} \quad (1)$$

The $Z_{90}(\lambda)$ was first calculated for the 173 spectra, followed by the computation of their mean and standard deviation spectrum (Fig. 2C).

Together with the tidal variability, the K_d will determine the amount of light that reaches the benthic substrate (Beer–Lambert law), with higher values meaning less light being transmitted to deeper layers, while it can also indicates roughly the maximum depth of occurrence of meadows (Duarte, 1991). The Z_{90} can be defined as the depth above which 90 % of light, i.e., the diffuse irradiance, is reflected (Gordon and McCluney, 1975), and its value indicates roughly the depth at which a sensor can obtain information from remote sensing, in optically deep waters. Lower values of Z_{90} (e.g., <1 m) were observed at shorter wavelengths in the blue (<460 nm) and in the near-infrared regions (>700 nm). The maximum value of Z_{90}, of approx. 2.3 m, was observed to be around 570 nm. It is important to note, however, the high variability of these parameters in the visible domain, i.e., from 400 to 700 nm, which reflects the importance of the seasonality in governing the optical properties. The seasonal aspect of the growth of nearshore vegetation should also be considered for mapping the intertidal meadows. During winter, the lower biomass of eelgrass and the presence of ice cover in the EGSL limits the ability to map eelgrass using optical remote sensing approaches. Moreover, at the beginning of the growing season (early May), the variability of reflectance values between different types of vegetation present in the intertidal zone is not significant, limiting their separability through multispectral imagery (Légaré et al., 2022). Therefore, the collection of images used in this study was constrained to the period from June to October.

Because of the limitations in accessing subtidal eelgrass meadows imposed by the variability of tides and water optical properties, only emerged (or non-flooded) pixels were considered for the classification procedure. Additionally, there are constraints imposed by the radiometry quality across Landsat sensors for water applications, which will be further discussed (Subsection 4.1). Nevertheless, from hereafter, the term *emerged* is defined by the tidally exposed portion of the shoal in the imagery and will be used throughout the text.

2.2. Repository, selection and pre-processing of images

The mapping of eelgrass meadows was conducted using the Landsat Collection 2 (C2) Tier 1 (T1) Level 2 Science Product (L2SP). This collection includes the satellites (sensors) Landsat 4, 5 (TM), 7 (ETM+), 8, and 9 (OLI), with surface reflectance (*SR*) products generated by the Land Surface Reflectance Code (LaSRC, for Landsat 8–9; USGS, 2023) and by the Landsat Ecosystem Disturbance Adaptive Processing System (LEDAPS, for Landsat 4–5, 7; Masek et al., 2006; USGS, 2021). The products are generated at a 30 m spatial resolution and cover a timespan of more than 40 years; they are fully available in the Google Earth Engine (GEE) catalog. From hereafter, the nomenclature used for each band and its corresponding wavelengths, for each collection, are those constant in the GEE Data Catalog.

Before processing the images in GEE, it was necessary to perform a primary delimitation of the polygons of the studied areas. This was accomplished using coastline extraction from satellite imagery and bathymetry from the Canadian Hydrographic Service (CHS) non-navigational (NONNA) bathymetric data. In short, the upper limit of the intertidal areas was determined using the Modified Normalized Difference Water Index (*MNDWI*; Xu 2006) applied to a recent Landsat image under high tide conditions. The MNDWI was calculated using the green and shortwave infrared 1 (SWIR 1) *SR* values as:

$$MNDWI = \frac{SR_{\text{Green}} - SR_{\text{SWIR 1}}}{SR_{\text{Green}} + SR_{\text{SWIR 1}}} \quad (2)$$

MNDWI values of approximately “0” were selected as a threshold to separate the nearshore zones (intertidal and adjacent subtidal) from land.

The outer (lower) limit of the primary delimitation of all subregions either used the 15 m isobath (BSI and MAN) or geomorphological features present along the coast, such as islands and promontories (RIB and IVE). An exploratory analysis of Landsat time-series imagery under low-tide conditions confirmed that the areas of interest included continuous eelgrass meadows and were suitable for classification using sensors with a 30 m spatial resolution. However, it is important to note that this primary delimitation does not represent the final intertidal areas considered in our analysis, as will be discussed next.

The polygons of the primary delimitation areas for the four subregions were uploaded to GEE and used to crop each Landsat scene (a methodological flowchart is shown in Fig. 3). After constraining the collection of images from June to October, the scaling factors were applied to each band (blue, green, red, near infrared, shortwave infrared 1, and shortwave infrared 2). Pixel quality attributes, namely the *Dilated Cloud* and *Cloud* attributes generated from the CFMASK algorithm (Zhu and Woodcock, 2012; Foga et al., 2017), were selected and used to flag the *SR* bands. The cropped images with more than 50 % of pixels masked by this procedure were discarded.

The next step consisted of extracting the emerged pixels polygons, which were performed using. a series of image-processing techniques implemented in GEE. The near-infrared (NIR) and SWIR bands are sensitive to flooded areas because of the high absorption of water in this spectral region, and the NIR band was found to be empirically related to tidal variability in the nearshore EGSL (data not shown). Therefore, this band was used as input to separate flooded and non-flooded areas. First, for noise removal, a spatial filter (convolve function in GEE) was applied using a Gaussian kernel with a radius equal to three pixels. The original and filtered

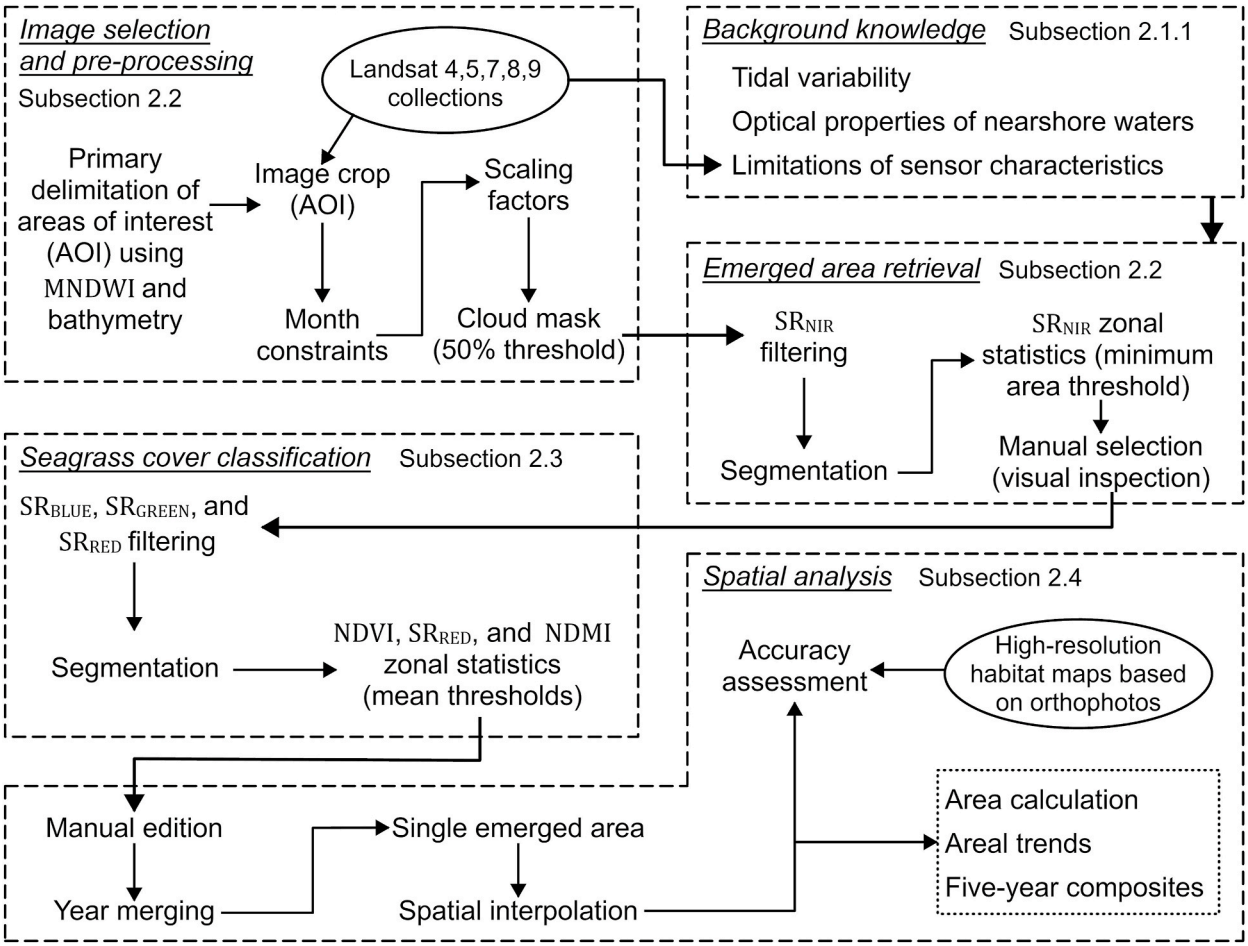

Fig. 3. Diagram of the process and analysis chain to assess the yearly and decadal variability of intertidal eelgrass meadow coverage in four subregions of the Estuary and Gulf of St. Lawrence. For each major step, the subsections where more detailed information is provided are also shown.

images were then subjected to a segmentation procedure, which consisted of superpixel clustering based on SNIC (simple non-iterative clustering; Achanta and Susstrunk, 2017), available in GEE. Zonal statistics, specifically the mean SR_{NIR} value of each segment, were computed, and a threshold of 0.05 was used to separate the emerged areas in each image of the collection. This procedure demonstrated good consistency with field observations and knowledge about shallow bathymetry.

Considering only the emerged areas from the resulting images, a minimum number of pixels was established as a threshold for selecting images having a reasonable emerged surface area. For example, an image with a lower number of pixels than the threshold value indicates that more pixels were considered flooded; therefore, it was not selected for the following classification. The thresholds varied by subregion and were empirically determined to ensure that a minimum number of images represented the yearly variability of intertidal eelgrass meadow coverage for the period between 1984 and 2023. Finally, a manual selection based on the visual inspection of individual images was made to avoid problems related to clouds that were not detected by the masking procedure (e.g., cirrus) and to ensure that no more than four images were selected in a single year.

The resulting polygons consisted of classes of *emerged* and *eelgrass* classes at an image basis resolution. Additional procedures for generating yearly and standardized spatial products for time series analysis are detailed in Subsection 2.4.

2.3. Eelgrass cover classification

As for the emerged areas delimitation, the polygons of eelgrass meadows were obtained through segmentation and classification by object-based image analysis. After conducting some tests using different combinations of bands, we found that using the blue, green and red bands in the filtering (Gaussian kernel) and segmentation (SNIC algorithm) processes yielded the best results. The zonal statistics (mean values in each segment) were computed for each *SR* and selected vegetation and water index. Similarly, after testing several indices, we found that the Normalized Difference Vegetation Index (*NDVI*; Tucker, 1979) and the Normalized Difference Moisture Index (*NDMI*; Wilson and Sader, 2002) were the most useful for discriminating the eelgrass polygons in intertidal EGSL zones.

The spectral indices are calculated as:

$$NDVI = \frac{SR_{NIR} - SR_{Red}}{SR_{NIR} + SR_{Red}} \quad (3)$$

$$NDMI = \frac{SR_{NIR} - SR_{SWIR\ 1}}{SR_{NIR} + SR_{SWIR\ 1}} \quad (4)$$

In short, the *NDVI* is used to assess vegetation greenness, whereas the *NDMI* is used to assess the moisture level of either soil or vegetation. The contrasting higher *NDVI* and lower SR_{Red} values of the meadows relative to surrounding bare sediment were effective in separating these two coverage types. Additionally, mean *NDMI* values were effective in distinguishing some salt marshes from eelgrass meadows. A possible explanation is the lower water content present in salt marshes at low tide than in eelgrass meadows.

Taking this into consideration, the classification of the eelgrass meadows was conducted through object-based image analysis, using the mean *NDVI*, SR_{Red}, and *NDMI* values of individual polygons (segments). The thresholds used in this rule-based classification scheme took the form of $NDVI \geq X$, "AND" $SR_{Red} \leq Y$, "AND" $NDMI \geq Z$. The threshold values were determined on a single-image basis, requiring more interaction within the classification process and user experience. The histogram of the threshold values is shown in Fig. S1A in the Supplementary Material 1 (S1; Appendix A). The variability of the mean values can be explained by oscillations of reflectance values that could be related to natural causes (vegetation phenology) or atmospheric correction issues and differences in solar viewing geometry.

The polygons classified as eelgrass and the total emerged areas of each image were exported from GEE, and some of them required manual editing. For example, isolated patches of known macroalgae beds were removed manually in the RIB and IVE subregions.

2.4. Eelgrass cover analysis and accuracy assessment

For each subregion, the resulting polygons of eelgrass patches and emerged areas were grouped and merged by year. The merging process considered the maximum area occupied by all polygons, incorporating both *eelgrass* and *no eelgrass* classes, for each year. The number of images per year varied from 1 to 4, and years without images were not considered in the analysis. An example of this procedure can be found in Fig. S2A in Supplementary Material 2 (S2).

A final emerged area was derived by considering that the same pixel location was classified as "emerged" at least 70 % of the total number of years analyzed (more information in S2 and Fig. S2B). This was a critical step in establishing a common baseline for comparison, across the entire time series. If the emerged area of a specific year did not cover the final (single) emerged area of the subregion, the missing areas were considered to be equal to the closest classified year (either *eelgrass* or *no eelgrass* classes, see the example in Fig. S2C).

The validation of the classification procedure was performed by direct comparison with maps of nearshore habitats based on orthophotos having a 30 cm spatial resolution (Jobin et al., 2021; SIGEC, 2023). The orthophotos, from Fisheries and Oceans Canada (DFO), were taken during low-tide conditions in September or October in the years 2015 (RIB and IVE) and 2016 (BSI and MAN) and were composed of four bands (RGB + NIR). In short, the orthophoto images were first submitted to a segmentation algorithm in PCI Geomatica software, and the segments were classified based on visual interpretation by experts, using oblique aerial photos and fieldwork recognition as auxiliary data. For the comparison, only the segments classified as predominantly eelgrass and with at least 25 % coverage were considered.

The spatial accuracy statistics were calculated through the computation of the confusion matrix (Congalton and Green, 2019), which was built considering the two classes and only in the final emerged area polygon for each subregion. The metrics include producer's accuracy (% of each reference class mapped correctly), user's accuracy (% of each map class that were correct in the reference), the overall accuracy (% of reference sites mapped correctly), and Cohen's kappa coefficient, which shows the strength of agreement between two variables (reference and mapped data), with 0 indicating no agreement, and 1 indicating complete agreement.

The final area of eelgrass meadows (per subregion and per year) was calculated by multiplying the number of classified pixels by the area of a unit pixel (equal to 900 m^2). Similarly, the percentage of the area covered by the meadows relative to the total emerged area was also calculated.

Temporal and spatial changes in eelgrass meadow coverage were assessed by grouping the yearly patches in five-years intervals, following a similar procedure to that used for of the yearly composition of the original classified images. The five-year composites were compared to 2023, which was selected as a reference year because it was the last year an image was classified. Meadows that were present at any time during the analyzed period but were not present in the reference year were also identified. Nevertheless, long-term trend analysis of the meadows was conducted by dividing the area of meadows (for each subregion and year) by their initial area (in 1984).

All image processing described in this subsection were made using MATLAB software (MathWorks®), and the final maps (presented as figures in this study) and the manual selection of polygons were created using ArcGIS Pro software (ESRI™).

3. Results

3.1. Image selection and classification accuracy

A total of 195 Landsat images were used to classify the coverage of eelgrass meadows in the four subregions. Supplementary

Table 1
Confusion matrix and accuracy assessment of eelgrass coverage. The values shown correspond to the sum of areas of all four subregions considered in this study.

Classified cover map (km^2)	Reference cover map (km^2)			User's accuracy (%)
	Eelgrass	No eelgrass	Total	
Eelgrass	33.70	1.84	35.54	95
No eelgrass	4.75	62.95	67.70	93
Total	38.45	64.79	103.24	
Producer's accuracy (%)	88	97		
Overall accuracy (%)	**94**		**$\kappa = 0.86$**	

The Cohen's kappa coefficient (κ) is presented separately and is out of context on the table.

Material 3 (S3) and Table S3A detail the selected Landsat imagery. The initial selection of images (cropped and monthly constrained; see Fig. 3) varied by subregion and was mainly related to the position of the areas of interest within the orbit (path and row) of the Landsat satellites. As a result, the L'Isle-Verte Bay (IVE) subregion had the highest number of images, whereas the other subregions had similar numbers (Table S3A). The application of the cloud mask threshold criteria (for image selection) reduced the initial selection by an average of 50 %. From this selection, the minimum area threshold applied to the classified emerged areas reduced the number of images by about 12 % in RIB, and by 36 % in IVE. This reduction testifies to the negative effect of high tidal levels on selecting images suitable for classification (the criterion of only emerged pixels). Manual selection removed between 16 % (IVE) and 27 % (BSI) of the remaining images.

The total surface area of the emerged polygons in the BSI, MAN, RIB, and IVE subregions was 20, 40, 12, and 31 km^2, respectively. The emerged polygons encompass most of the intertidal zone of each subregion, with relatively smaller intertidal and adjacent subtidal areas omitted in the following analysis. It is important to note that the threshold used to separate the emerged pixels may also include very shallow (<1 m) submerged areas, because the reflectance signals of the bottom in the NIR band may not be negligeable (see Fig. 2C), and especially where submerged aquatic vegetation is present (which has higher NIR reflectance). Moreover, these areas may be also included in the analysis due to intra-pixel mixing or to inaccuracies in the thresholding method.

The confusion matrix and accuracy assessment results, analyzed by comparing the classes *eelgrass* and *no eelgrass* coverage of the year correspondent to the ecosystem mapping based on aerial photographs and in situ observations, are presented in Table 1. The areas presented in Table 1 consider the sum of the four subregions. An overall accuracy of 94 % and a kappa coefficient (κ) of 0.86 reveal a very good agreement for classification. More importantly, the accuracy assessment exercise ensured that the classification procedure developed in this study classified meadows with at least 25 % areal coverage, as estimated by photointerpretation of the aerial photographs. Furthermore, as the general image-processing procedures were systematic for the entire Landsat time series, we assume that the classification procedure was valid for the whole analyzed period.

The degree of misclassification areas varied by subregion (see Table S4A, in Supplementary Material 4 [S4]) and mainly related to regions where eelgrass meadows were mixed with other vegetation types and where their coverage was close to 25 %. For example, in the BSI subregion (overall accuracy: 86 % and $\kappa = 0.62$), a sector known to have sparse eelgrass coverage (approx. 25 % in the reference map) was not classified in the Landsat workflow. These types of misclassifications were present to a lesser degree in the other subregions (overall accuracy >90 % and $\kappa > 0.8$). Nonetheless, misclassifications at the edge of the polygons were also observed and attributed to the discrepancy of two orders of magnitude between the spatial resolution of Landsat (30 m) and the aerial photographs (30 cm) used in the reference maps.

3.2. Eelgrass coverage, area, trends, and changes

The analysis of eelgrass coverage in the intertidal zone of the studied areas (subregions) revealed its highly dynamic nature at yearly and decadal time scales. Fig. 4 shows selected Landsat images from the approximate initial year of analysis and the approximate year of maximum coverage for each subregion. A clear trend is the abrupt increase, in all subregions, of the area occupied by the meadows relative to bare sediment (or meadows with less coverage), when comparing recent years images from the 1980s.

The shape and area of the emerged zones retrieved from the processing chain reflected the major geomorphological aspects of each subregion. The emerged area in BSI followed the shape of the bay and varied from about 1 to 2.5 km in width. Two major types of emerged areas were observed in the MAN subregion. The first, associated with the peninsula feature of the coastline and corresponding to half of the total emerged area, presented a typical width of about 1 km and was the main area of eelgrass occurrence. The second type, which made up the other half, is associated with the deltas of the Aux-Outardes and Manicouagan rivers, while being less occupied by eelgrass meadows. Nevertheless, the emerged areas of RIB and IVE occupied the zones between land and the barrier islands, sometimes forming a contiguous area reaching up to 3 km wide (e.g., for the RIB subregion).

The temporal evolution of areal cover of the meadows and their respective relative occupation of the emerged zone (in percentage) is presented in Fig. 5. In all subregions, the initial area of the meadows (in 1984) was the lowest in the entire period and was 1 km^2 or less (except for IVE, which had an initial area of approx. 1.5 km^2). All subregions experienced a significant increase in meadow coverage over the years, reaching the highest areas in the BSI and IVE subregions (almost 17 km^2) in 2020 and 2022, respectively. The largest area for RIB was observed at the end of the time series (2023), reaching approximately 2.5 km^2. In contrast, the MAN subregion

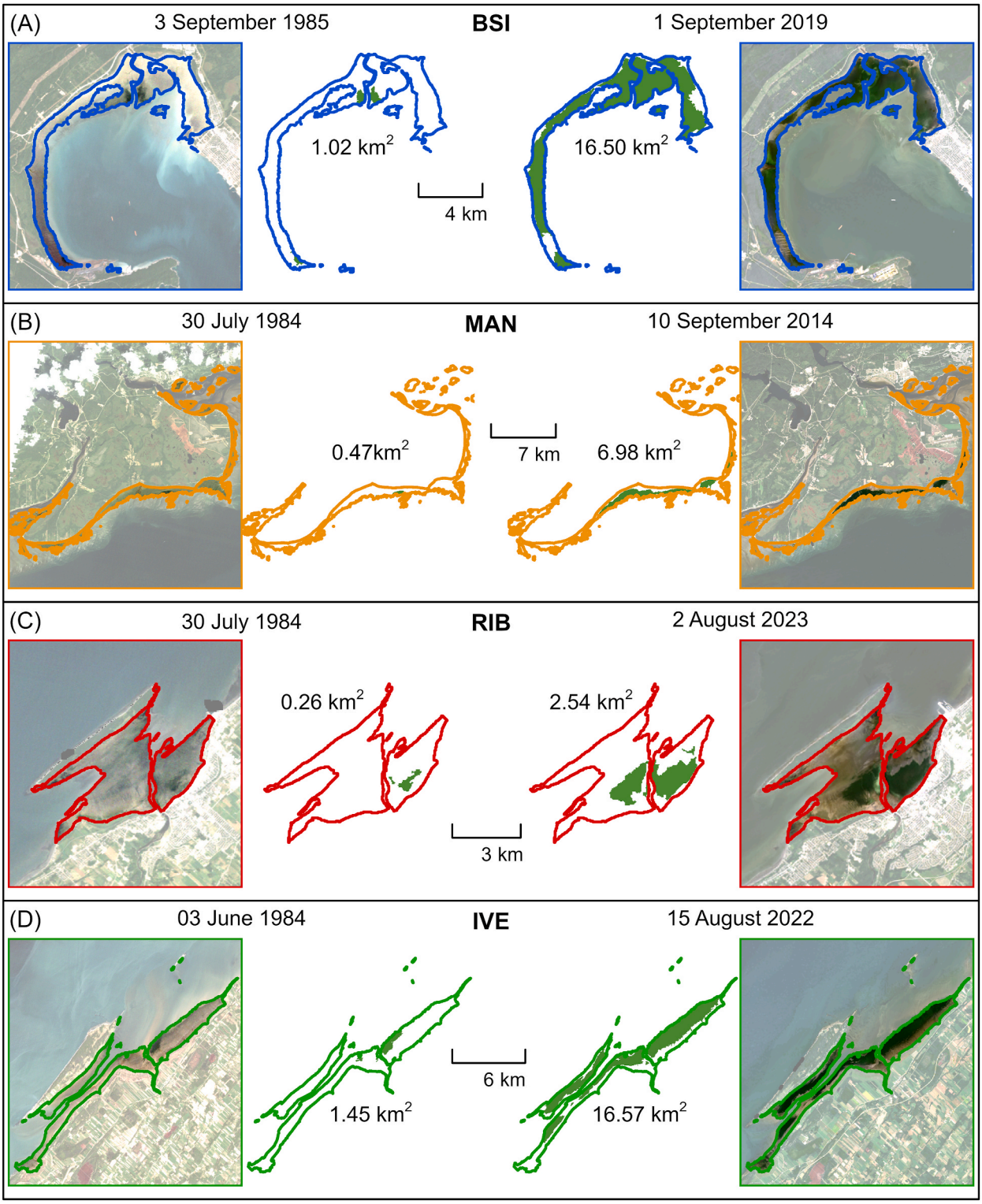

Fig. 4. Examples of Landsat images used in the classification process of eelgrass meadows (*green patches*) inside the polygons of the emerged areas (*solid lines* with varying colors for subregions: blue, BSI; yellow, MAN; red, RIB; green, IVE). Images in the left-hand column correspond to the approximately years of minimum area of meadows, whereas the right-hand column presents the approximately years of maximum extent.

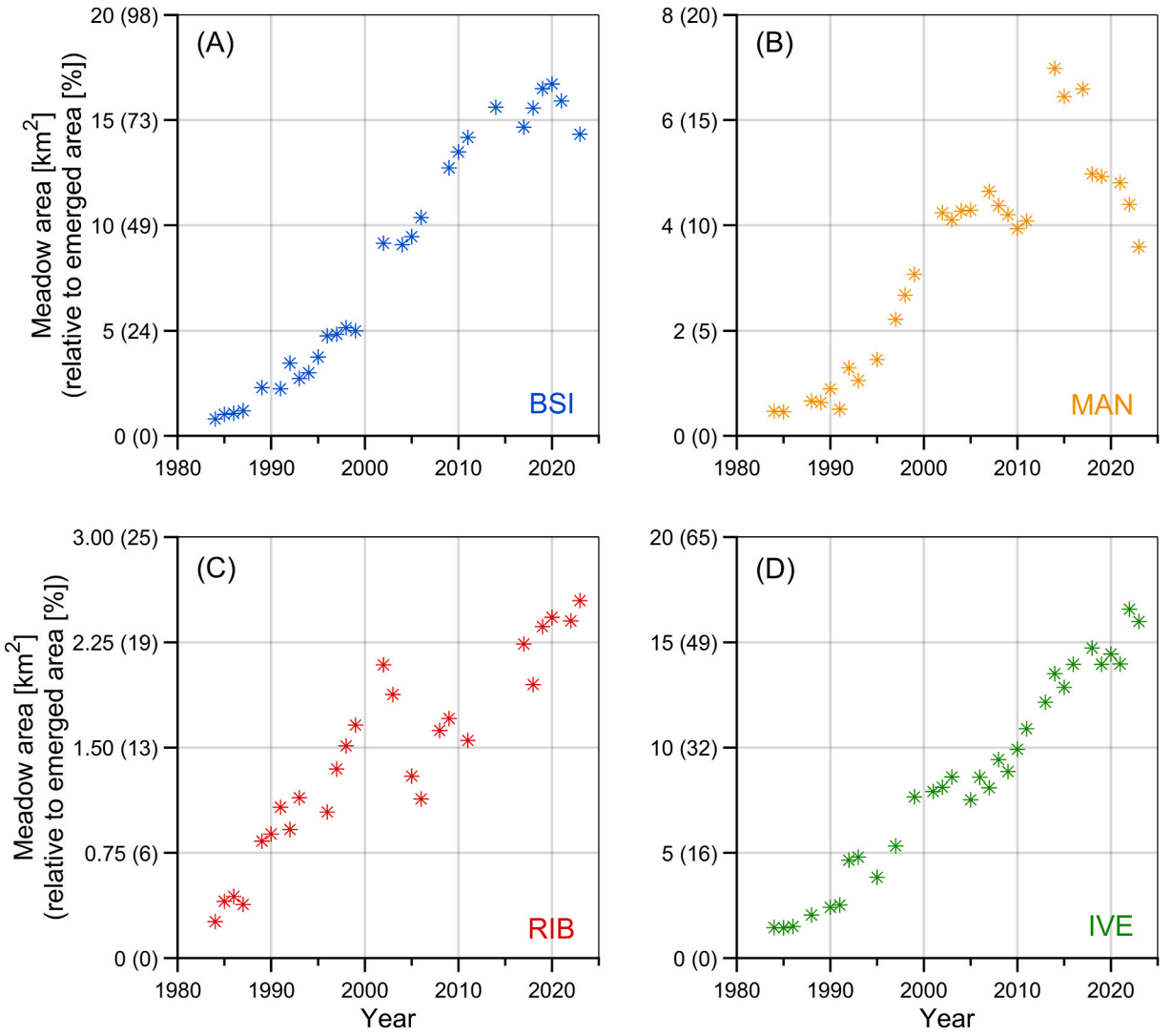

Fig. 5. Temporal evolution of areal cover of eelgrass meadows in the four subregions (A to D). The values in parentheses along the *y-axis* are the percentage of the eelgrass areal cover in relation to the total emerged area. The color codes for the subregions are the same as in Fig. 4.

reached its maximum in 2014 (6.7 km^2), followed by an almost linear decline since (approx. 3.5 km^2 loss from 2014 to 2023). Meadows in the BSI subregion decreased in area from 2020. It is important to note the differences of the absolute area of the meadows (y-axis in Fig. 5) among subregions, which maximum values ranged from 2.5 to 16.7 km^2, for RIB and BSI, respectively. Small fluctuations in the areal increase trends were observed throughout the entire time series for all subregions. A decrease was also noted from 2002 to 2006 in RIB (1 km^2 loss), followed by significant growth until 2023. A relatively stable state was observed between 2000 and 2010 in the MAN and IVE subregions.

The percentage of meadow coverage relative to total emerged areas (values in parentheses in Fig. 5) also varied by subregion. The BSI presented the highest value of relative coverage, reaching 82 % of the total emerged area in 2020. In contrast, the meadow coverage in the MAN and RIB subregions reached only 17 %–22 % of the intertidal emerged area, whereas IVE presented an intermediate relative coverage, with a value of approximately 54 %. In contrast, the initial relative cover of all subregions was below 5 % in 1984. These results indicate a relative saturation of space in the emerged areas of the BSI subregion for eelgrass expansion, considering that some areas are also occupied by salt marshes. The lower relative occupation rate of meadows in the MAN subregion can be associated with the high proportion of the emerged areas being present in more dynamic locations, such as river deltas and sandbanks subject to migration.

To complement the quantitative trends in eelgrass cover, we provide spatial distribution maps for each subregion (Fig. 6). These maps illustrate the evolution of eelgrass extent over selected years and offer a more intuitive visualization of the spatial dynamics driving the observed areal changes. By maintaining a consistent scale across all panels, the figure enables direct comparison of temporal patterns between subregions and highlights the variability in expansion or contraction of eelgrass meadows over time.

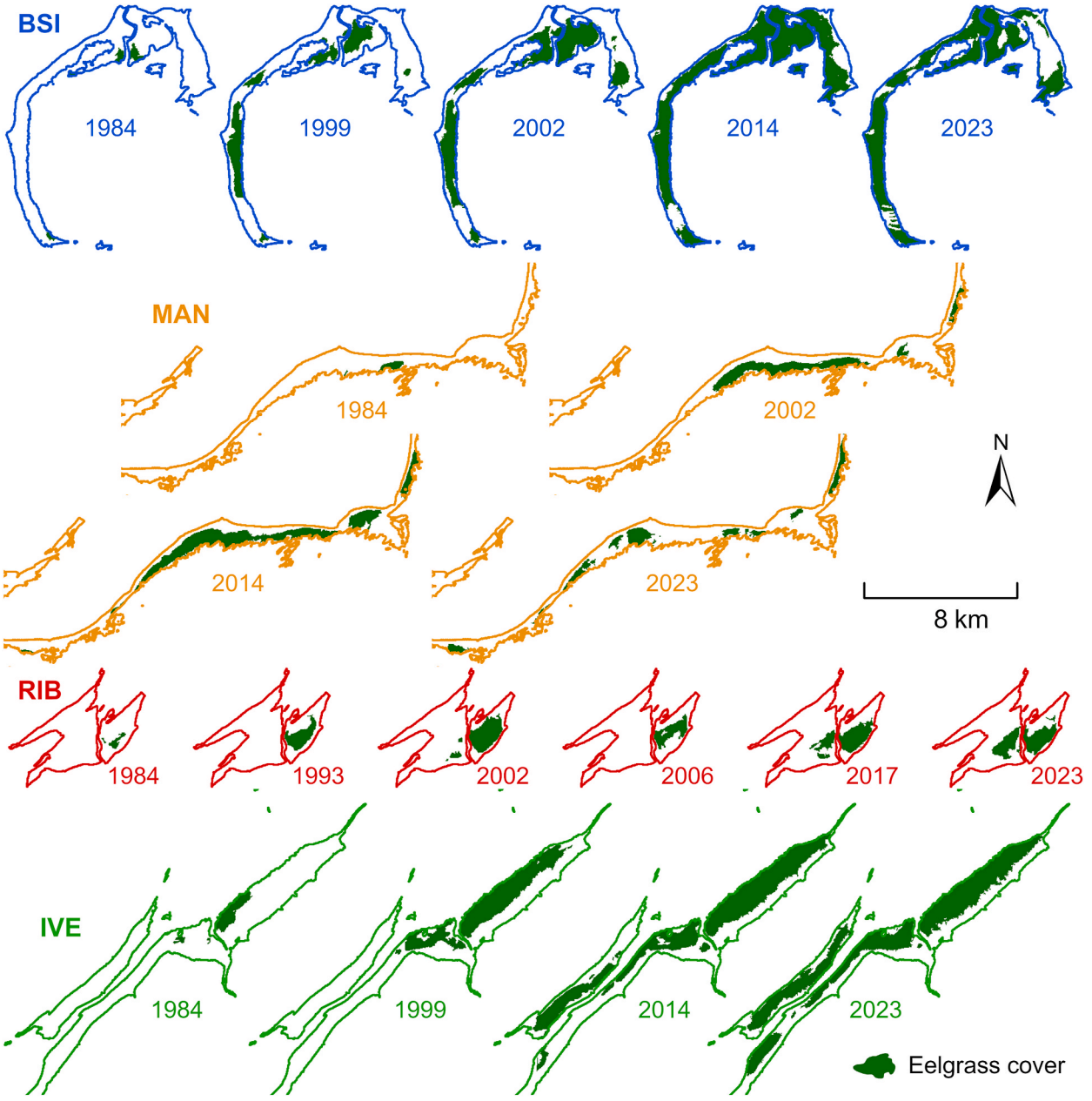

Fig. 6. Representative spatial distribution maps of eelgrass polygons over time in each of the four EGSL subregions. The maps illustrate temporal changes in eelgrass coverage across selected benchmark years. The color codes for the subregions are the same as in Fig. 4.

The seagrass areal trends for the EGSL are plotted in Fig. 7. The yearly areal eelgrass coverage was normalized by the initial area (1984) for comparison between subregions. The solid line curves were obtained by fitting a 4th degree polynomial equation to the log10-transformed data, illustrating the relative areal trends in the four subregions relative to the 1984 data. For comparison, the curves from the North Atlantic Ocean, from both the east and west coasts (world bioregions; Short et al., 2007), compiled by Dunic et al. (2021) are presented. The general trends were very similar for all subregions, reaching as much as a 21-fold increase for BSI and a 10-fold increase or higher for the other subregions. Compared to global bioregional trends, the EGSL eelgrass meadows experienced about an order of magnitude higher increase than in the northeastern Atlantic (European coasts). This expansion trend in the EGSL was opposite to that of southern northwestern Atlantic meadows (see Fig. 1 of Dunic et al., 2021).

The spatial dynamics of eelgrass meadow expansion over the last decades are shown in Figs. 8 and 9. The comparison of a reference year (i.e., 2023) with the coverage over the decades allowed for the identification of when and where the meadows first appeared (or disappeared). In general, the expansion started in small patches and was located mostly closer to the lower limit of the emerged areas (i.e., lower intertidal limit, near the subtidal fringe in an offshore direction). Thus, the expansion generally started in areas farthest

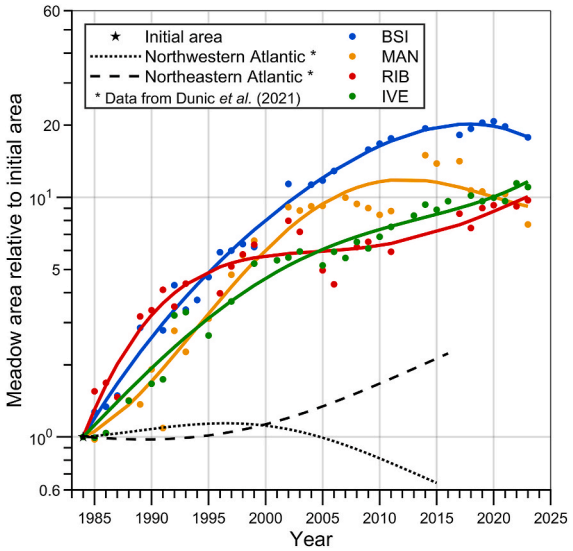

Fig. 7. Eelgrass meadows areal trends in the Estuary and Gulf of St. Lawrence over the last four decades and in comparison with other seagrass areal trends along the northeastern Atlantic (western Europe) and northwestern Atlantic (eastern North America) coasts.

from the coast and expanded landward. This spatial pattern was more evident in the BSI and MAN subregions, along the north coast of the EGSL. Moreover, areas where the meadows were present at any time during the analyzed period, but for some reason disappeared (relative to the reference year), are also shown in Figs. 8 and 9 as light red patches. Specifically, these "lost" patches in the MAN and RIB subregions correspond to the abovementioned recent decline and is shown in the areal evolution (Fig. 5).

4. Discussion

The spatial variability of eelgrass meadows on an annual to decadal time frame was investigated for the first time in the Estuary and Gulf of St. Lawrence (EGSL), one of the largest estuarine systems in the world. In this section, we first discuss the advent of cloud-computing and availability of collections for automated processing of extensive image data, as well as some limitations. Secondly, we discuss the observed trajectories of the seagrass meadows in EGSL compared to trajectories worldwide. Finally, we draw some hypotheses that could explain the expansion of the intertidal meadows.

4.1. Cloud-computing and imagery repository

The retrieval of seagrass coverage was performed using Landsat historical images processed with the Google Earth Engine (GEE) cloud-computing platform. The advent of GEE, together with the availability of optical imagery archives, has allowed several seagrass mapping efforts around the world, either involving time-series analysis (e.g., Lizcano-Sandoval et al., 2022; Sebastian et al., 2023) or actual inventories (e.g., Kovacs et al., 2022; Traganos et al., 2022a; b; Li et al., 2022) of areal coverage. Combining cloud computing and the availability of imagery repositories makes it possible to map very large areas at relatively low computational costs; thus, estimates of the areal coverage of seagrass meadows are easier. Moreover, the availability of analysis-ready data through GEE-like repositories provides access to a large number of images and favors their use by end users, while at the same time minimizing the need for more complicated image-processing techniques, such as atmospheric correction procedures. However, it is important to note that high spatial resolution (<30 m) products specifically designed for water color applications would benefit not only the retrieval of water quality parameters but also assist recovering optically shallow benthic coverage information, including seagrass mapping.

In addition to the dynamic nature of tides and water optical properties affecting the meadows and complicating their mapping, another physical constraint to consider is the inherent limitations of Landsat sensors. Although the 30 m spatial resolution and similar spectral resolutions (similar center wavelengths but varying bandwidths) are maintained across the different Landsat sensor generations, there have been significant improvements in radiometric quality from the Landsat 4 Thematic Mapper (TM) to the Landsat 9 Operational Land Imager (OLI). The TM and the Enhanced Thematic Mapper Plus (ETM+) sensors have 8-bit quantization, whereas OLI has 12 and 14 bits for Landsat 8 and 9, respectively.

This increase in radiometric precision improves overall signal-to-noise ratios (SNRs) and enhances the performance of algorithms for earth science applications (Schott et al., 2016). Specifically, the lower radiometric quality of TM and ETM+ sensors implies poor atmospheric correction performance to retrieve surface reflectance (or remote sensing reflectance) for water color applications (Xu et al., 2020; Maciel et al., 2023). Consequently, the information on eelgrass meadows that are flooded by tides is also compromised. Moreover, the low reflectance values of the nearshore waters of the EGSL attributed to their strongly light-absorbing and weakly light-scattering nature (Araújo and Bélanger, 2022), pose challenges for the application of atmospheric correction methods, even for

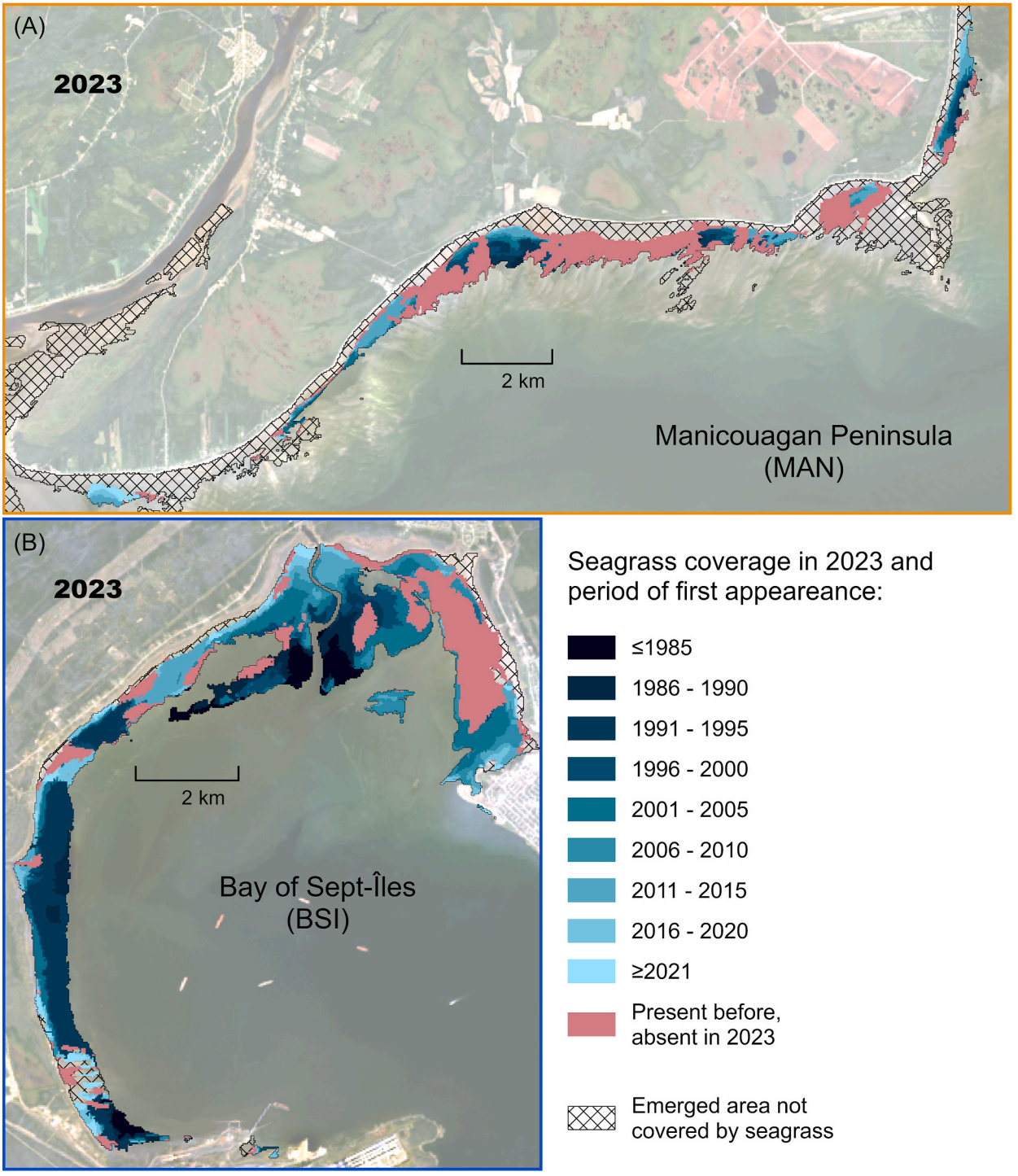

Fig. 8. Decadal spatial changes of eelgrass patches in the (A) MAN and (B) BSI subregions of the Estuary and Gulf of St. Lawrence.

advanced Landsat 8 OLI or Sentinel 2 MSI sensors (see Mabit et al., 2022). Notwithstanding, the legacy of the Landsat continuity program provides a unique opportunity to establish a baseline of seagrass distribution at yearly to decadal temporal scales, as demonstrated by several studies (Dekker et al., 2005; Gullström et al., 2006; Lyons et al., 2013; Calleja et al., 2017; Fernandes et al., 2022).

Although there are inherent limitations to accessing subtidal seagrass in highly absorbing and turbid waters with TM and ETM+ sensors, advances in the capabilities of satellite and airborne sensors have proven adequate to overcome or minimize this issue

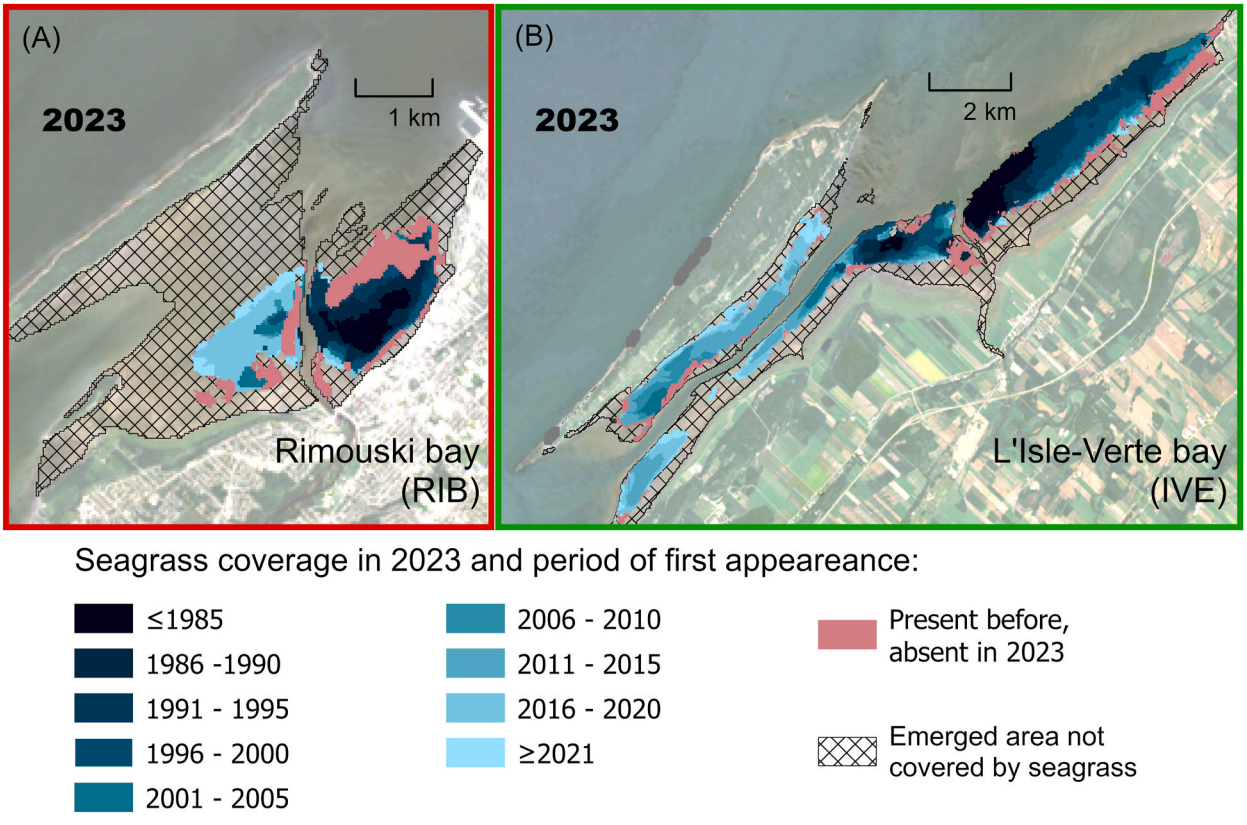

Fig. 9. Decadal spatial changes of eelgrass patches in the (A) RIB and (B) IVE subregions of the Estuary and Gulf of St. Lawrence.

(Dierssen et al., 2019; Krause et al., 2021; Kuhwald et al., 2022). Therefore, recent and planned satellite missions hold promise for extrapolating the mapping of eelgrass meadows in subtidal areas of the EGSL, if water clarity allows for the physical detection of the bottom.

4.2. Spatial and temporal trajectories of seagrass meadows

We observed a significant increase in the areal coverage of meadows in intertidal areas in four contrasting subregions of the EGSL. The general trend was similar among the subregions on the decadal scale. However, these trends are not linear considering the interannual variability, with measured losses of meadows coverage in some subregions.

Limiting the classification to exposed macrophytes in low-tide conditions present advantages and is a common procedure applied to optical imagery (e.g.; Zoffoli et al., 2020; Carlson et al., 2023). Restricting the analysis to intertidal areas reduce uncertainties produced by variability in water optical properties and sun and sky glint and permits classifying eelgrass meadows through the application of land-based vegetation indices. Nevertheless, knowledge of the spectral signatures of the various types of coverage occurring in the tidal flats is a primary requirement for developing classification tools (see Davies et al., 2023). It is important to note, however, the limitations of multispectral imagery, such as the ones provided by Landsat sensors, in discriminating between different types of vegetation (e.g., seagrass and macroalgae), as observed in some intertidal areas of the EGSL (e.g., Légaré et al., 2022).

Since our analysis was limited to the most exposed (emerged) intertidal areas, we assessed the areal cover of meadows occupying the outer limit of the intertidal and shallow subtidal areas of each subregion. These areas were also retrieved from the nearshore habitat maps used in the validation procedure (Jobin et al., 2021; SIGEC, 2023), while it corresponds to a snapshot of the whole time series, relative to the year of acquisition of the orthophotos. The area of the meadows was 15.72, 17.19, 0.03, and 4.18 km^2, for BSI, MAN, RIB, and IVE, respectively. These values reveal that the area occupied by subtidal seagrass is very significant. This was more evident in MAN, with the area of the subtidal meadows being 2.5 times higher than the area occupied by the meadows in the emerged area. For BSI, the area of the meadows in the two zones were approximately equal. On the south shore of the EGSL, the subtidal areal cover of the meadows was less significant, with ~33 % of the emerged meadows in IVE, and almost no meadows outside the emerged zone (<2 %) in RIB. Interestingly, the subregions more exposed to the main body of the EGSL presented the highest proportion of subtidal meadows coverage. For example, in the IVE subregion, almost all meadows coverage in the outer limit of the intertidal and subtidal conditions correspond to its northeastern part, where the coast is not sheltered by the island, comparatively to other parts.

While areas beyond the emerged polygons could be captured in certain Landsat images, even including those from the TM and

ETM+ sensors, the definition of a common analysis area was essential to ensure methodological consistency across the time series. However, this analysis can be considered in future inventories, which could be favored by the larger number of missions and sensors characteristics, as previously discussed. Notwithstanding, the "colonization depth of seagrass," i.e., the light-limited maximum depth to which seagrass grows (Beck et al., 2018b), is strictly related to irradiance levels reaching the underwater benthic substrate (Dennison et al., 1993; Ralph et al., 2007). Thus, combining the retrieval of water quality parameters such as the diffuse attenuation coefficient (e.g., $K_d(PAR)$) with photoacclimation and light thresholds of seagrass would facilitate access to the knowledge of the depth limits of the meadows.

The eelgrass meadows coverage in the EGSL increased markedly over the last four decades, contrary to global declining trends and particularly when compared to previous inventories in the temperate northwestern Atlantic (Waycott et al., 2009; Dunic et al., 2021). Our results reveal the recolonization of the tidal flats since 1984, a shift from the catastrophic decline at the end of the 1920s caused by the wasting disease, establishing these nearshore zones of the EGSL as ecologically significant habitats (*Zostera marina* was recognized as an "ecologically significant species" in Canada; Fisheries and Oceans Canada, DFO, 2009). This recovery trend in seagrass meadow coverage has been reported in a few recent studies along the temperate northeastern Atlantic coast (western Europe) (de los Santos et al., 2019), the eastern shore of Virginia (Orth et al., 2020), southwest Florida (Tomasko et al., 2018; Lizcano-Sandoval et al., 2022), and South Australia (Fernandes et al., 2022). Overall, these studies associate such increases with an overall improvement in water quality (less nutrient input in coastal areas leading to less eutrophication and turbid conditions) and the relative success of transplantation programs (e.g., Orth et al., 2020). Although a few localized eelgrass transplant initiatives were identified within our study areas—particularly in the IVE subregion in the early 1990s (see Lalumière 1991)—these isolated efforts are insufficient to explain the broader increase observed in this subregion, which followed the general trend of other areas in the EGSL.

An overall increase in the coverage of dwarf eelgrass (*Z. noltei* Hornemann) has also been observed in intertidal areas of northeastern Atlantic (Bourgneuf Bay, France, approx. 46°60′N; Zoffoli et al., 2021). In this case, and for the intertidal eelgrass meadows of the EGSL, light limitation caused by overlaying waters during high tide is unlikely because subaerial conditions may satisfy the light requirements for seagrass growth (for example, see Cussioli et al., 2019).

The trajectories of eelgrass meadow coverage in cold temperate and subarctic environments vary greatly within regions. In Canada, the quantification of temporal changes in the area of eelgrass meadows remains incomplete (Murphy et al., 2021). In James Bay (a water body located in Arctic-like conditions), eelgrass meadows experienced a major decline in between 1995 and 1999, followed by a limited recovery (Leblanc et al., 2023). In Atlantic Canada, about 69 % of the eelgrass meadows sites have shown either a stable, restored, or increasing trend, whereas 31 % showed a decline (Murphy et al., 2021). For example, a region in the southern Gulf of St. Lawrence (Tabusintac Estuary) has exhibited a relatively stable subtidal meadows coverage over more than three decades (Leblanc et al., 2021). The nearshore areas contemplated in our study are separated by up to 300 km of distance from each other (BSI and IVE); nonetheless they showed a consistent and significant areal increase. Even with relatively contrasting coastal setups and oceanographic conditions (see Supplementary Material 5 [S5] and Table S5A for more information), meadows in the four subregions of the EGSL presented similar increasing trajectories (see Fig. 7).

Within the overall increase over the 40 years, we noted marked interannual variability. This was particularly evident in the losses of meadows in the BSI, MAN, and RIB subregions. In general, the increase (or recovery) pattern was slower than the loss, which was often more abrupt. We observed a similar pattern in Bourgneuf Bay for the intertidal dwarf eelgrass (Zoffoli et al., 2021). However, the gradual loss in eelgrass extent observed for the MAN subregion during the last decade calls for more attention. Moreover, the MAN subregion is that most exposed to hydrodynamic agents. These observations highlight the need to understand the mechanisms driving short-term losses and recovery and to identify the role of local environmental variables.

4.3. Potential factors contributing to the dynamics of seagrass meadow coverage in EGSL

Several testable hypotheses can be proposed to explain the increase in the meadows observed along the 40 years; they include the causal responses to the reduction in ice cover (e.g., Krause-Jensen and Duarte, 2014), adaptation to changes in mean relative sea level (e.g., Kairis and Rybczyk, 2010; Kirwan and Megonigal, 2013), and shifts in the temperature towards the optimal range of growth (e.g., Lee et al., 2007). However, a single environmental variable or factor may not be adequate to explain the observed changes, as eelgrass responds differently when subjected to multiple stressors (Lefcheck et al., 2017; Cimon et al., 2021; Dunic and Côté, 2023).

In regards to the interannual variability of the meadows coverage, various local processes can be listed, such as the exposure of the meadows to wave action, the intensity and frequency of storms, the burial of seagrass meadows by the migration of sandbars and high sedimentation rates (e.g., Mills and Fonseca, 2003; Hirst et al., 2017), along with the phenology and dynamics of the ice foot (e.g., Robertson and Mann, 1984). Notwithstanding, both decadal and interannual processes need further investigation.

5. Conclusion

The spatial extent of eelgrass in the Estuary and Gulf of St. Lawrence (EGSL) was documented for the first time over both decadal and interannual timescales. A marked expansion in areal coverage was observed, ranging from a tenfold increase (approximately 0.3–2.5 km^2) to a twenty-one-fold increase (approximately 0.8–16.7 km^2). This expansion is likely to have significant ecological implications. In particular, the proliferation of eelgrass meadows plays a critical role in enhancing shoreline stabilization (Marin-Diaz et al., 2020) and supporting (blue) carbon storage (Marbà et al., 2018; Röhr et al., 2018).

The methodology developed in this study demonstrates strong potential for transferability to other intertidal environments, particularly those with similar benthic characteristics. Mapping and tracking the evolution of coastal and nearshore habitats is critical

because these areas are often biodiversity hotspots and provide essential ecosystem services, including serving as nursery grounds for fisheries, providing coastal protection, and contributing to carbon sequestration. In this context, Earth Observation Technologies offer a powerful tool for researchers, coastal managers and stakeholders.

Looking ahead, the use of recent satellite missions such as Sentinel-2 and ICESat-2 presents a valuable opportunity to extend this work to submerged eelgrass beds in the Gulf of St. Lawrence, including those in Baie-des-Chaleurs and the lagoons of Îles-de-la-Madeleine. While these technologies do not offer historical perspectives, they significantly enhance spatial and temporal resolution, enabling the assessment of interannual and even seasonal variability in eelgrass dynamics. In addition, satellite-derived bathymetry can serve as a key asset by providing high-resolution depth information in shallow coastal waters, supporting more accurate mapping of eelgrass distribution and habitat suitability.

The increasing areal extent of eelgrass meadows in EGSL over the last four decades suggests a major regional control and, as for the short interannual variability, requires further investigation of the environmental variables driving this change and their interactive effects of multiple stressors.

CRediT authorship contribution statement

Carlos A.S. Araújo: Writing – review & editing, Writing – original draft, Visualization, Software, Methodology, Formal analysis, Data curation, Conceptualization. **Simon Bélanger:** Writing – review & editing, Funding acquisition, Conceptualization. **Pascal Bernatchez:** Writing – review & editing, Funding acquisition, Conceptualization. **Mathieu Cusson:** Writing – review & editing, Funding acquisition, Conceptualization.

Data statement

The data used in this work consists of freely available Landsat imagery generated by the United States Geological Survey (USGS) and accessible through the Google Earth Engine (GEE) platform. Ecosystem maps of reference are available online through the SIGEC web (https://ldgizc.uqar.ca/Web/sigecweb).

Ethical statement

The authors declare that all ethical practices have been followed in relation to the development, writing and publication of the work reported in this paper.

Funding

This research is a contribution to the Canadian Healthy Oceans Network (CHONe-2), funded by the Natural Sciences and Engineering Research Council of Canada (NSERC) in partnership with Fisheries and Oceans Canada and INREST (representing the Port of Sept-Îles and City of Sept-Îles); and the WISE-Man Project (WaterSat Imaging Spectrometer Experiment [WISE] for Optically Shallow Inland and Coastal Waters Assessment), funded by the Canadian Space Agency through the FAST program (18FARIMA20), Fisheries and Oceans Canada through the Coastal Environmental Baseline Program (2018-032-QC-UQAR-Bélanger), and Québec-Ocean. This work was partly supported by Réseau Québec maritime (RQM - request number: 2017-38-09) awarded to MC; NSERC Discovery grants (MC: RGPIN-2017-05525; SB: RGPIN-2019-0670). CA was supported by PhD scholarships from the Fond de Recherche du Québec – Nature et technologies (FRQNT), through a grant from the Merit Scholarship Program for Foreign Students (https://doi.org/10.69777/263427), CHONe-2, and RQM.

Declaration of competing interest

The authors declare that they have no known competing financial interests or personal relationships that could have appeared to influence the work reported in this paper.

Acknowledgments

The authors would like to thank Dr. Jillian Dunic for sharing the data provided in Fig. 7, and Drs. Michel Gosselin, Jean-Éric Tremblay, Christian Nozais, Laura Zoffoli and two anonymous reviewers for providing useful comments and reviewing early versions of this manuscript.

Appendix A. Supplementary Material

Supplementary material to this article can be found online at https://doi.org/10.1016/j.rsase.2025.101623.

Data availability

Shapefiles representing seagrass distributions for each surveyed year, as well as the emerged areas analyzed in each subregion, are publicly available via GitHub/Zenodo at https://doi.org/10.5281/zenodo.15643391. An example of the GEE code used in the analysis is also included at the same repository.

References

Achanta, R., Susstrunk, S., 2017. Superpixels and polygons using simple non-iterative clustering. IEEE, pp. 4895–4904. https://doi.org/10.1109/CVPR.2017.520.

Araújo, C.A.S., Bélanger, S., 2022. Variability of bio-optical properties in nearshore waters of the estuary and Gulf of St. Lawrence: absorption and backscattering coefficients. Estuar. Coast Shelf Sci. 264, 107688. https://doi.org/10.1016/j.ecss.2021.107688.

Araújo, C.A.S., Belzile, C., Tremblay, J.-É., Bélanger, S., 2022. Environmental niches and seasonal succession of phytoplankton assemblages in a subarctic coastal bay: applications to remote sensing estimates. Front. Mar. Sci. 9, 1001098. https://doi.org/10.3389/fmars.2022.1001098.

Beck, M.W., Heck, K.L., Able, K.W., Childers, D.L., Eggleston, D.B., Gillanders, B.M., Halpern, B., Hays, C.G., Hoshino, K., Minello, T.J., Orth, R.J., Sheridan, P.F., Weinstein, M.P., 2001. The identification, conservation, and management of estuarine and marine nurseries for fish and invertebrates. Bioscience 51, 633–641. https://doi.org/10.1641/0006-3568(2001)051[0633:TICAMO]2.0.CO;2.

Beck, H.E., Zimmermann, N.E., McVicar, T.R., Vergopolan, N., Berg, A., Wood, E.F., 2018a. Present and future Köppen-Geiger climate classification maps at 1-km resolution. Sci. Data 5, 180214. https://doi.org/10.1038/sdata.2018.214.

Beck, M.W., Hagy, J.D., Le, C., 2018b. Quantifying seagrass light requirements using an algorithm to spatially resolve depth of colonization. Estuaries Coasts 41, 592–610. https://doi.org/10.1007/s12237-017-0287-1.

Boström, C., Jackson, E.L., Simenstad, C.A., 2006. Seagrass landscapes and their effects on associated fauna: a review. Estuar. Coast Shelf Sci. 68, 383–403. https://doi.org/10.1016/j.ecss.2006.01.026.

Calleja, F., Galván, C., Silió-Calzada, A., Juanes, J.A., Ondiviela, B., 2017. Long-term analysis of *Zostera noltei*: a retrospective approach for understanding seagrasses' dynamics. Mar. Environ. Res. 130, 93–105. https://doi.org/10.1016/j.marenvres.2017.07.017.

Carlson, D.F., Vivó-Pons, A., Treier, U.A., Mätzler, E., Meire, L., Sejr, M., Krause-Jensen, D., 2023. Mapping intertidal macrophytes in fjords in Southwest Greenland using Sentinel-2 imagery. Sci. Total Environ. 865, 161213. https://doi.org/10.1016/j.scitotenv.2022.161213.

Cimon, S., Deslauriers, A., Cusson, M., 2021. Multiple stressors and disturbance effects on eelgrass and epifaunal macroinvertebrate assemblage structure. Mar. Ecol. Prog. Ser. 657, 93–108. https://doi.org/10.3354/meps13546.

Congalton, R.G., Green, K., 2019. Assessing the Accuracy of Remotely Sensed Data, third ed. CRC Press, 346 p. https://doi.org/10.1201/9780429052729.

Cussioli, M.C., Bryan, K.R., Pilditch, C.A., de Lange, W.P., Bischof, K., 2019. Light penetration in a temperate meso-tidal lagoon: implications for seagrass growth and dredging in Tauranga Harbour, New Zealand. Ocean Coast Manag. 174, 25–37. https://doi.org/10.1016/j.ocecoaman.2019.01.014.

Davies, B.F.R., Gernez, P., Geraud, A., Oiry, S., Rosa, P., Zoffoli, M.L., Barillé, L., 2023. Multi- and hyperspectral classification of soft-bottom intertidal vegetation using a spectral library for coastal biodiversity remote sensing. Remote Sens. Environ. 290, 113554. https://doi.org/10.1016/j.rse.2023.113554.

de los Santos, C.B., Krause-Jensen, D., Alcoverro, T., Marbà, N., Duarte, C.M., van Katwijk, M.M., Pérez, M., Romero, J., Sánchez-Lizaso, J.L., Roca, G., Jankowska, E., Pérez-Lloréns, J.L., Fournier, J., Montefalcone, M., Pergent, G., Ruiz, J.M., Cabaço, S., Cook, K., Wilkes, R.J., Moy, F.E., Traiter, G.M.-R., Arañ o, S., de Jong, D.J., Fernández-Torquemada, Y., Auby, I., Vergara, J.J., Santos, R., 2019. Recent trend reversal for declining European seagrass meadows. Nat Commun 10, 3356. https://doi.org/10.1038/s41467-019-11340-4.

Dekker, A.G., Brando, V.E., Anstee, J.M., 2005. Retrospective seagrass change detection in a shallow coastal tidal Australian lake. Remote Sens. Environ. 97, 415–433. https://doi.org/10.1016/j.rse.2005.02.017.

Den Hartog, C., 1987. "Wasting disease" and other dynamic phenomena in Zostera beds. Aquat. Bot. 27, 3–14. https://doi.org/10.1016/0304-3770(87)90082-9.

Dennison, W.C., Orth, R.J., Moore, K.A., Stevenson, J.C., Carter, V., Kollar, S., Bergstrom, P.W., Batiuk, R.A., 1993. Assessing water quality with submersed aquatic vegetation. Bioscience 43, 86–94. https://doi.org/10.2307/1311969.

Dierssen, H.M., Bostrom, K.J., Chlus, A., Hammerstrom, K., Thompson, D.R., Lee, Z., 2019. Pushing the limits of seagrass remote sensing in the turbid waters of Elkhorn Slough, California. Remote Sens. 11, 13–15. https://doi.org/10.3390/rs11141664.

Duarte, C.M., 1991. Seagrass depth limits. Aquat. Bot. 40, 363–377. https://doi.org/10.1016/0304-3770(91)90081-F.

Duarte, C.M., 2017. Reviews and syntheses: hidden forests, the role of vegetated coastal habitats in the ocean carbon budget. Biogeosciences 14, 301–310. https://doi.org/10.5194/bg-14-301-2017.

Duarte, B., Martins, I., Rosa, R., Matos, A.R., Roleda, M.Y., Reusch, T.B.H, Engelen, A.H., Serrão, E.A., Pearson, G.A., Marques, J.C., Caçador, I., Duarte, C.M., Jeterbock, A., 2018. Climate change impacts on seagrass meadows and macroalgal forests: an integrative perspective on acclimation and adaptation potential. Front. Mar. Sci. 5. https://doi.org/10.3389/fmars.2018.00190.

Duffy, J., 2006. Biodiversity and the functioning of seagrass ecosystems. Mar. Ecol. Prog. Ser. 311, 233–250. https://doi.org/10.3354/meps311233.

Dunic, J.C., Côté, I.M., 2023. Management thresholds shift under the influence of multiple stressors: eelgrass meadows as a case study. Conserv. Lett. 1–9. https://doi.org/10.1111/conl.12938.

Dunic, J.C., Brown, C.J., Connolly, R.M., Turschwell, M.P., Côté, I.M., 2021. Long-term declines and recovery of meadow area across the world's seagrass bioregions. Glob. Change Biol. 27, 4096–4109. https://doi.org/10.1111/gcb.15684.

El-Sabh, M.I., Murty, T.S., 1990. Mathematical modelling of tides in the St. Lawrence estuary. In: El-Sabh, M., Silverberg, N. (Eds.), Oceanography of a Large-Scale Estuarine System, pp. 10–50. https://doi.org/10.1007/978-1-4615-7534-4_2.

El-Sabh, M.I., Silverberg, N., 1990. In: El-Sabh, M.I., Silverberg, N. (Eds.), Oceanography of a Large-Scale Estuarine System. Springer, New York. https://doi.org/10.1007/978-1-4615-7534-4.

El-Sabh, M.I., Lie, H.-J., Koutitonsky, V.G., 1982. Variability of the near-surface residual current in the lower St. Lawrence estuary. J. Geophys. Res. 87, 9589. https://doi.org/10.1029/JC087iC12p09589.

Fernandes, M.B., Hennessy, A., Law, W.B., Daly, R., Gaylard, S., Lewis, M., Clarke, K., 2022. Landsat historical records reveal large-scale dynamics and enduring recovery of seagrasses in an impacted seascape. Sci. Total Environ. 813, 152646. https://doi.org/10.1016/j.scitotenv.2021.152646.

Ferrario, F., Araújo, C.A.S., Bélanger, S., Bourgault, D., Carrière, J., Carrier-Belleau, C., Dreujou, E., Johnson, L.E., Juniper, S.K., Mabit, R., McKindsey, C.W., Ogston, L., Picard, M.M.M., Saint-Louis, R., Saulnier-Talbot, E., Shaw, J.-L., Templeman, N., Therriault, T.W., Tremblay, J.-E., Archambault, P., 2022. Holistic environmental monitoring in ports as an opportunity to advance sustainable development, marine science, and social inclusiveness. Elem. Sci. Anthr. 10, 1–21. https://doi.org/10.1525/elementa.2021.00061.

Fisheries and Oceans Canada, (DFO), 2009. Does eelgrass (Zostera marina) meet the criteria as an ecologically significant species? Can. Sci. Advis. Secr. Sci. Advis. Rep. 2009/018 11 https://waves-vagues.dfo-mpo.gc.ca/library-bibliotheque/337549.pdf.

Foga, S., Scaramuzza, P.L., Guo, S., Zhu, Z., Dilley, Beckmann, T., Schimidt, G.L., Dwyer, J.L., Hughes, M.J., Laue, B., 2017. Cloud detection algorithm comparison and validation for operational Landsat data products. Remote Sens. Environ. 194, 379–390. https://doi.org/10.1016/j.rse.2017.03.026.

Gallagher, A.J., Brownscombe, J.W., Alsudairy, N.A., Casagrande, A.B., Fu, C., Harding, L., Harris, S.D., Hammerschlag, N., Howe, W., Delgado Huertas, A., Kattan, S., Kough, A.S., Musgrove, A., Payne, N.L., Phillips, A., Shea, B.D., Shipley, O.N., Sumaila, U.R., Hossain, M.S., Duarte, C.M., 2022. Tiger sharks support the characterization of the world's largest seagrass ecosystem. Nat. Commun. 13, 6328. https://doi.org/10.1038/s41467-022-33926-1.

Gordon, H.R., McCluney, W.R., 1975. Estimation of the depth of sunlight penetration in the sea for remote sensing. Appl. Opt. 14, 413. https://doi.org/10.1364/AO.14.000413.

Gorelick, N., Hancher, M., Dixon, M., Ilyushchenko, S., Thau, D., Moore, R., 2017. Google earth engine: planetary-scale geospatial analysis for everyone. Remote Sens. Environ. 202, 18–27. https://doi.org/10.1016/j.rse.2017.06.031.

Grech, A., Chartrand-Miller, K., Erftemeijer, P., Fonseca, M., McKenzie, L., Rasheed, M., Taylor, H., Coles, R., 2012. A comparison of threats, vulnerabilities and management approaches in global seagrass bioregions. Environ. Res. Lett. 7, 024006. https://doi.org/10.1088/1748-9326/7/2/024006.

Gullström, M., Lundén, B., Bodin, M., Kangwe, J., Öhman, M.C., Mtolera, M.S.P., Björk, M., 2006. Assessment of changes in the seagrass-dominated submerged vegetation of tropical Chwaka Bay (Zanzibar) using satellite remote sensing. Estuar. Coast Shelf Sci. 67, 399–408. https://doi.org/10.1016/j.ecss.2005.11.020.

Hemminga, M.A., Duarte, C.M., 2000. Seagrasses in the human environment. In: Seagrass Ecology. Cambridge University Press, pp. 248–291. https://doi.org/10.1017/CBO9780511525551.008.

Henderson, C.J., Stevens, T., Lee, S.Y., Gilby, B.L., Schlacher, T.A., Connolly, R.M., Warnken, J., Maxwell, P.S., Olds, A.D., 2019. Optimising seagrass conservation for ecological functions. Ecosystems (N. Y.) 22, 1368–1380. https://doi.org/10.1007/s10021-019-00343-3.

Hirst, A.J., McGain, S., Jenkins, G.P., 2017. The impact of burial on the survival and recovery of the subtidal seagrass *Zostera nigricaulis*. Aquat. Bot. 142, 10–15. https://doi.org/10.1016/j.aquabot.2017.06.001.

Holmer, M., 2019. Productivity and biogeochemical cycling in seagrass ecosystems. In: Perillo, G.M.E., Wolanski, E., Cahoon, D.R., Hopkinson, C.S. (Eds.), Coastal Wetlands: an Integrated Approach. Elsevier, pp. 443–477. https://doi.org/10.1016/B978-0-444-63893-9.00013-7.

Hossain, M.S., Hashim, M., 2019. Potential of Earth Observation (EO) technologies for seagrass ecosystem service assessments. Int. J. Appl. Earth Obs. Geoinf. 77, 15–29. https://doi.org/10.1016/j.jag.2018.12.009.

Jayathilake, D.R.M., Costello, M.J., 2018. A modelled global distribution of the seagrass biome. Biol. Conserv. 226, 120–126. https://doi.org/10.1016/j.biocon.2018.07.009.

Jobin, A., Marquis, G., Provencher-Nolet, L., Gabaj Castrillo. M. J., Trubiano C., Drouet, M., Eustache-Létourneau, D., Drejza, S. Fraser, C. Marie, G. et P. Bernatchez (2021) Cartographie des écosystèmes côtiers du Québec maritime — Rapport méthodologique. Chaire de recherche en géoscience côtière, Laboratoire de dynamique et de gestion intégrée des zones côtières, Université du Québec à Rimouski. Rapport remis au ministère de l'Environnement et de la Lutte contre les changements climatiques, septembre 2021, 98 p. https://ldgizc.uqar.ca/Web/docs/default-source/default-document-library/cartographieecosystemes_final91273fac36d54462b9c26819b805ad9d.pdf?sfvrsn=871a3bf4_2.

Kairis, P.A., Rybczyk, J.M., 2010. Sea level rise and eelgrass (*Zostera marina*) production: a spatially explicit relative elevation model for Padilla Bay, WA. Ecol. Model. 221, 1005–1016. https://doi.org/10.1016/j.ecolmodel.2009.01.025.

Kirwan, M.L., Megonigal, J.P., 2013. Tidal wetland stability in the face of human impacts and sea-level rise. Nature 504, 53–60. https://doi.org/10.1038/nature12856.

Kovacs, E.M., Roelfsema, C., Udy, J., Baltais, S., Lyons, M., Phinn, S., 2022. Cloud processing for simultaneous mapping of seagrass meadows in optically complex and varied water. Remote Sens. 14, 1–9. https://doi.org/10.3390/rs14030609.

Krause, J.R., Hinojosa-Corona, A., Gray, A.B., Watson, E.B., 2021. Emerging sensor platforms allow for seagrass extent mapping in a turbid estuary and from the meadow to ecosystem scale. Remote Sens. 13, 1–15. https://doi.org/10.3390/rs13183681.

Krause-Jensen, D., Duarte, C.M., 2014. Expansion of vegetated coastal ecosystems in the future Arctic. Front. Mar. Sci. 1. https://doi.org/10.3389/fmars.2014.00077.

Kuhwald, K., Schneider von Deimling, J., Schubert, P., Oppelt, N., 2022. How can Sentinel-2 contribute to seagrass mapping in shallow, turbid Baltic Sea waters? Remote Sens. Ecol. Conserv. 8, 328–346. https://doi.org/10.1002/rse2.246.

Lalumière, R., 1991. Essais de transplantation de zostère marine à L'Isle-Verte, Québec (1990). Rapp. présenté au Serv. Can. la faune. Environ. Canada 42+5 p. https://publications.gc.ca/collections/collection_2024/eccc/cw66/CW66-1454-1991-fra.pdf.

Leblanc, M.-L., LaRocque, A., Leblon, B., Hanson, A., Humphries, M.M., 2021. Using Landsat time-Series to monitor and inform seagrass dynamics: a case study in the Tabusintac estuary, New Brunswick, Canada. Can. J. Rem. Sens. 47, 65–82. https://doi.org/10.1080/07038992.2021.1893672.

Leblanc, M.-L., O'Connor, M.I., Kuzyk, Z.Z.A., Noisette, F., Davis, K.E., Rabbitskin, E., Sam, L.-L., Neumeier, U., Costanzo, R., Ehn, J.K., Babb, D., Idrobo, C.J., Gilbert, J.-P., Leblon, B., Humphries, M.M., 2023. Limited recovery following a massive seagrass decline in subarctic eastern Canada. Glob. Change Biol. 29, 432–450. https://doi.org/10.1111/gcb.16499.

Lee, K.S., Park, S.R., Kim, Y.K., 2007. Effects of irradiance, temperature, and nutrients on growth dynamics of seagrasses: a review. J. Exp. Mar. Biol. Ecol. 350, 144–175. https://doi.org/10.1016/j.jembe.2007.06.016.

Lefcheck, J.S., Wilcox, D.J., Murphy, R.R., Marion, S.R., Orth, R.J., 2017. Multiple stressors threaten the imperiled coastal foundation species eelgrass (Zostera marina) in Chesapeake Bay, USA. Glob. Change Biol. 23, 3474–3483. https://doi.org/10.1111/gcb.13623.

Légaré, B., Bélanger, S., Singh, R.K., Bernatchez, P., Cusson, M., 2022. Remote sensing of coastal vegetation phenology in a cold temperate intertidal system: implications for classification of coastal habitats. Remote Sens. 14, 3000. https://doi.org/10.3390/rs14133000.

Li, Q., Jin, R., Ye, Z., Gu, J., Dan, L., He, J., Christakos, G., Agusti, S., Duarte, C.M., Wu, J., 2022. Mapping seagrass meadows in coastal China using GEE. Geocarto Int 37, 12602–12617. https://doi.org/10.1080/10106049.2022.2070672.

Lizcano-Sandoval, L., Anastasiou, C., Montes, E., Raulerson, G., Sherwood, E., Muller-Karger, F.E., 2022. Seagrass distribution, areal cover, and changes (1990–2021) in coastal waters off West-Central Florida, USA. Estuar. Coast Shelf Sci. 279, 108134. https://doi.org/10.1016/j.ecss.2022.108134.

Lotze, H.K., Lenihan, H.S., Bourque, B.J., Bradbury, R.H., Cooke, R.G., Kay, M.C., Kidwell, S.M., Kirby, M.X., Peterson, C.H., Jackson, J.B.C., 2006. Depletion, degradation, and recovery potential of estuaries and coastal seas. Science 312, 1806–1809. https://doi.org/10.1126/science.1128035.

Lyons, M.B., Roelfsema, C.M., Phinn, S.R., 2013. Towards understanding temporal and spatial dynamics of seagrass landscapes using time-series remote sensing. Estuar. Coast Shelf Sci. 120, 42–53. https://doi.org/10.1016/j.ecss.2013.01.015.

Mabit, R., Araújo, C.A.S., Singh, R.K., Bélanger, S., 2022. Empirical remote sensing algorithms to retrieve SPM and CDOM in québec coastal waters. Front. Remote Sens. 3, 834908. https://doi.org/10.3389/frsen.2022.834908.

Maciel, D.A., Pahlevan, N., Barbosa, C.C.F., de Novo, E.M.L.d.M., Paulino, R.S., Martins, V.S., Vermote, E., Crawford, C.J., 2023. Validity of the Landsat surface reflectance archive for aquatic science: implications for cloud-based analysis. Limnol. Oceanogr. Lett. 8, 850–858. https://doi.org/10.1002/lol2.10344.

Marbà, N., Krause-Jensen, D., Masqué, P., Duarte, C.M., 2018. Expanding Greenland seagrass meadows contribute new sediment carbon sinks. Sci. Rep. 8, 14024. https://doi.org/10.1038/s41598-018-32249-w.

Marin-Diaz, B., Bouma, T.J., Infantes, E., 2020. Role of eelgrass on bed-load transport and sediment resuspension under oscillatory flow. Limnol. Oceanogr. 65, 426–436. https://doi.org/10.1002/lno.11312.

Masek, J.G., Vermote, E.F., Saleous, N.E., Wolfe, R., Hall, F.G., Huemmrich, K.F., Gao, F., Kutler, J., Lim, T.-K., 2006. A Landsat surface reflectance dataset for North America, 1990–2000. Geosci. Rem. Sens. Lett. IEEE 3, 68–72. https://doi.org/10.1109/LGRS.2005.857030.

McKenzie, L.J., Nordlund, L.M., Jones, B.L., Cullen-Unsworth, L.C., Roelfsema, C., Unsworth, R.K.F., 2020. The global distribution of seagrass meadows. Environ. Res. Lett. 15, 074041. https://doi.org/10.1088/1748-9326/ab7d06.

Michaud, R., 1985. La mousse de mer : de L'Isle-Verte à la Baie des Chaleurs. Leméac, p. 221. https://lemeac.com/livres/la-mousse-de-mer-de-lisle-verte-a-la-baie-des-chaleurs/.

Mills, K., Fonseca, M., 2003. Mortality and productivity of eelgrass *Zostera marina* under conditions of experimental burial with two sediment types. Mar. Ecol. Prog. Ser. 255, 127–134. https://doi.org/10.3354/meps255127.

Moore, K.A., 2004. Influence of seagrasses on water quality in shallow regions of the lower Chesapeake Bay. J. Coast Res. 10045, 162–178. https://doi.org/10.2112/SI45-162.1.

Muehlstein, L.K., Porter, D., Short, F.T., 1991. *Labyrinthula zosterae Sp. Nov.* , the causative agent of wasting disease of eelgrass, *Zostera marina*. Mycologia 83, 180–191. https://doi.org/10.1080/00275514.1991.12025994.

Murphy, G.E.P., Dunic, J.C., Adamczyk, E.M., Bittick, S.J., Côté, I.M., Cristiani, J., Geissinger, E.A., Gregory, R.S., Lotze, H.K., O'Connor, M.I., Araújo, C.A.S., Rubidge, E.M., Templeman, N.D., Wong, M.C., 2021. From coast to coast to coast: ecology and management of seagrass ecosystems across Canada. FACETS 6, 139–179. https://doi.org/10.1139/facets-2020-0020.

Ondiviela, B., Losada, I.J., Lara, J.L., Maza, M., Galván, C., Bouma, T.J., van Belzen, J., 2014. The role of seagrasses in coastal protection in a changing climate. Coast. Eng. 87, 158–168. https://doi.org/10.1016/j.coastaleng.2013.11.005.

Orth, R.J., Carruthers, T.J.B., Dennison, W.C., Duarte, C.M., Fourqurean, J.W., Heck, K.L., Hughes, A.R., Kendrick, G.A., Kenworthy, W.J., Olyarnik, S., Short, F.T., Waycott, M., Williams, S.L., 2006. A global crisis for seagrass ecosystems. Bioscience 56, 987–996. https://doi.org/10.1641/0006-3568(2006)56[987:AGCFSE]2.0.CO;2.

Orth, R.J., Lefcheck, J.S., McGlathery, K.S., Aoki, L., Luckenbach, M.W., Moore, K.A., Oreska, M.P.J., Snyder, R., Wilcox, D.J., Lusk, B., 2020. Restoration of seagrass habitat leads to rapid recovery of coastal ecosystem services. Sci. Adv. 6, 1–9. https://doi.org/10.1126/sciadv.abc6434.

Provencher, L., Deslandes, S., 2012. Utilisation d'images satellitaires pour évaluer la superficie, l'étendue et la densité de l'herbier de la zostère marine (*Zostera marina*) de la péninsule de Manicouagan (Québec). Rapp. tech. can. sci. halieut. aquat. 2988: vi + 16 pp https://publications.gc.ca/collections/collection_2012/mpo-dfo/Fs97-6-2988-fra.pdf.

Quintin, C., Bernatchez, P., Buffin-Bélanger, T., 2006. Géomorphologie et diversité végétale des marais du Cap Marteau et de l'Isle-Verte, estuaire du Saint-Laurent, Québec. Géogr. Phys. Quaternaire 60, 149–164. https://doi.org/10.7202/016826ar.

Ralph, P.J., Durako, M.J., Enríquez, S., Collier, C.J., Doblin, M.A., 2007. Impact of light limitation on seagrasses. J. Exp. Mar. Biol. Ecol. 350, 176–193. https://doi.org/10.1016/j.jembe.2007.06.017.

Robertson, A.I., Mann, K.H., 1984. Disturbance by ice and life-history adaptations of the seagrass *Zostera marina*. Mar. Biol. 80, 131–141. https://doi.org/10.1007/BF02180180.

Röhr, M.E., Holmer, M., Baum, J.K., Björk, M., Boyer, K., Chin, D., Chalifour, L., Cimon, S., Cusson, M., Dahl, M., Deyanova, D., Duffy, J.E., Eklöf, J.S., Geyer, J.K., Griffin, J.N., Gullström, M., Hereu, C.M., Hori, M., Hovel, K.A., Hughes, A.R., Jorgensen, P., Kiriakopolos, S., Moksnes, P.-O., Nakaoka, M., O'Connor, M.I., Peterson, B., Reiss, K., Reynolds, P.L., Rossi, F., Ruesink, J., Santos, R., Stachowicz, J.J., Tomas, F., Lee, K.-S., Unsworth, R.K.F., Boström, C., 2018. Blue carbon storage capacity of temperate eelgrass (*Zostera marina*) meadows. Glob. Biogeochem. Cycles 32, 1457–1475. https://doi.org/10.1029/2018GB005941.

Schott, J.R., Gerace, A., Woodcock, C.E., Wang, S., Zhu, Z., Wynne, R.H., Blinn, C.E., 2016. The impact of improved signal-to-noise ratios on algorithm performance: case studies for Landsat class instruments. Remote Sens. Environ. 185, 37–45. https://doi.org/10.1016/j.rse.2016.04.015.

Sebastian, T., Sreenath, K.R., Sreeram, M.P., Ranith, R., 2023. Dwindling seagrasses: a multi-temporal analysis on Google earth engine. Ecol. Inform. 74, 101964. https://doi.org/10.1016/j.ecoinf.2022.101964.

Shaw, J.-L., Bourgault, D., Dumont, D., Lefaivre, D., 2022. Hydrodynamics of the bay of Sept-Îles. Atmos.-Ocean 0, 1–17. https://doi.org/10.1080/07055900.2022.2141605.

Short, F.T., Ibelings, B.W., Den Hartog, C., 1988. Comparison of a current eelgrass disease to the wasting disease in the 1930s. Aquat. Bot. 30, 295–304. https://doi.org/10.1016/0304-3770(88)90062-9.

Short, F., Carruthers, T., Dennison, W., Waycott, M., 2007. Global seagrass distribution and diversity: a bioregional model. J. Exp. Mar. Biol. Ecol. 350, 3–20. https://doi.org/10.1016/j.jembe.2007.06.012.

SIGEC, 2023. Système intégré de gestion de l'environnement côtier (SIGEC Web). Laboratoire de dynamique et gestion intégrée des zones côtières. Available at: https://ldgizc.uqar.ca/Web/sigecweb.

Therriault, J.-C., Legendre, L., Demers, S., 1990. Oceanography and ecology of phytoplankton in the St.Lawrence estuary. In: El-Sabh, M., Silverberg, N. (Eds.), Oceanography of a Large-Scale Estuarine System, pp. 269–295. https://doi.org/10.1007/978-1-4615-7534-4_12.

Tomasko, D., Alderson, M., Burnes, R., Hecker, J., Leverone, J., Raulerson, G., Sherwood, E., 2018. Widespread recovery of seagrass coverage in Southwest Florida (USA): temporal and spatial trends and management actions responsible for success. Mar. Pollut. Bull. 135, 1128–1137. https://doi.org/10.1016/j.marpolbul.2018.08.049.

Traganos, D., Lee, C.B., Blume, A., Poursanidis, D., Čižmek, H., Deter, J., Mačić, V., Montefalcone, M., Pergent, G., Pergent-Martini, C., Ricart, A.M., Reinartz, P., 2022a. Spatially explicit seagrass extent mapping across the entire mediterranean. Front. Mar. Sci. 9. https://doi.org/10.3389/fmars.2022.871799, 871799.

Traganos, D., Pertiwi, A.P., Lee, C.B., Blume, A., Poursanidis, D., Shapiro, A., 2022b. Earth observation for ecosystem accounting: spatially explicit national seagrass extent and carbon stock in Kenya, Tanzania, Mozambique and Madagascar. Remote Sens Ecol Conserv 8, 778–792. https://doi.org/10.1002/rse2.287.

Tucker, C.J., 1979. Red and photographic infrared linear combinations for monitoring vegetation. Remote Sens. Environ. 8, 127–150. https://doi.org/10.1016/0034-4257(79)90013-0.

Turner, M.G., 1989. Landscape ecology: the effect of pattern on process. Annu. Rev. Ecol. Systemat. 20, 171–197. https://doi.org/10.1146/annurev.es.20.110189.001131.

Unsworth, R.K.F., Collier, C.J., Waycott, M., Mckenzie, L.J., Cullen-Unsworth, L.C., 2015. A framework for the resilience of seagrass ecosystems. Mar. Pollut. Bull. 100, 34–46. https://doi.org/10.1016/j.marpolbul.2015.08.016.

Unsworth, R.K.F., McKenzie, L.J., Collier, C.J., Cullen-Unsworth, L.C., Duarte, C.M., Eklöf, J.S., Jarvis, J.C., Jones, B.L., Nordlund, L.M., 2018. Global challenges for seagrass conservation. Ambio 48, 801–815. https://doi.org/10.1007/s13280-018-1115-y.

Unsworth, R.K.F., Nordlund, L.M., Cullen-Unsworth, L.C., 2019b. Seagrass meadows support global fisheries production. Conserv. Lett. 12, e12566. https://doi.org/10.1111/conl.12566.

USGS, 2021. Landsat 4-7 Level 2 Science Product (L2SP) Guide. p. 38 LSDS-1618. Available at: https://www.usgs.gov/media/files/landsat-4-7-collection-2-level-2-science-product-guide.

USGS, 2023. Landsat 8-9 Level 2 Science Product (L2SP) Guide. p. 37 LSDS-1619. Available at: https://www.usgs.gov/media/files/landsat-8-9-collection-2-level-2-science-product-guide.

Veettil, B.K., Ward, R.D., Lima, M.D.A.C., Stankovic, M., Hoai, P.N., Quang, N.X., 2020. Opportunities for seagrass research derived from remote sensing: a review of current methods. Ecol. Indic. 117, 106560. https://doi.org/10.1016/j.ecolind.2020.106560.

Waycott, M., Duarte, C.M., Carruthers, T.J.B., Orth, R.J., Dennison, W.C., Olyarnik, S., Calladine, A., Fourqurean, J.W., Heck Jr., K.L., Hughes, A.R., Kendrick, G.A., Kenworthy, W.J., Short, F.T., Williams, S.L., 2009. Accelerating loss of seagrasses across the globe threatens coastal ecosystems. Proc. Natl. Acad. Sci. 106, 12377–12381. https://doi.org/10.1073/pnas.0905620106.

Whitfield, A.K., 2017. The role of seagrass meadows, mangrove forests, salt marshes and reed beds as nursery areas and food sources for fishes in estuaries. Rev. Fish Biol. Fish. 27, 75–110. https://doi.org/10.1007/s11160-016-9454-x.

Wilson, E.H., Sader, S.A., 2002. Detection of forest harvest type using multiple dates of Landsat TM imagery. Remote Sens. Environ. 80, 385–396. https://doi.org/10.1016/S0034-4257(01)00318-2.

Wulder, M.A., Roy, D.P., Radeloff, V.C., Loveland, T.R., Anderson, M.C., Johnson, D.M., Healey, S., Zhu, Z., Scambos, T.A., Pahlevan, N., Hansen, M., Gorelick, N., Crawford, C.J., Masek, J.G., Hermosilla, T., White, J.C., Belward, A.S., Schaaf, C., Woodcock, C.E., Huntington, J.L., Lymburner, L., Hostert, P., Gao, F., Lyapustin, A., Pekel, J.-F., Strobl, P., Cook, B.D., 2022. Fifty years of Landsat science and impacts. Remote Sens. Environ. 280, 113195. https://doi.org/10.1016/j.rse.2022.113195.

Xu, H., 2006. Modification of normalised difference water index (NDWI) to enhance open water features in remotely sensed imagery. Int. J. Rem. Sens. 27, 3025–3033. https://doi.org/10.1080/01431160600589179.

Xu, Y., Feng, L., Zhao, D., Lu, J., 2020. Assessment of Landsat atmospheric correction methods for water color applications using global AERONET-OC data. Int. J. Appl. Earth Obs. Geoinf. 93, 102192. https://doi.org/10.1016/j.jag.2020.102192.

Zhu, Z., Woodcock, C.E., 2012. Object-based cloud and cloud shadow detection in Landsat imagery. Remote Sens. Environ. 118, 83–94. https://doi.org/10.1016/j.rse.2011.10.028.

Zoffoli, M.L., Gernez, P., Rosa, P., Le Bris, A., Brando, V.E., Barillé, A.-L., Harin, N., Peters, S., Poser, K., Spaias, L., Peralta, G., Barillé, L., 2020. Sentinel-2 remote sensing of *Zostera noltei*-dominated intertidal seagrass meadows. Remote Sens. Environ. 251, 112020. https://doi.org/10.1016/j.rse.2020.112020.

Zoffoli, M.L., Gernez, P., Godet, L., Peters, S., Oiry, S., Barillé, L., 2021. Decadal increase in the ecological status of a North-Atlantic intertidal seagrass meadow observed with multi-mission satellite time-series. Ecol. Indic. 130, 108033. https://doi.org/10.1016/j.ecolind.2021.108033.